Stellar kinematics in surveys and simulations

DANIEL MIKKOLA
DEPT. OF ASTRONOMY AND THEORETICAL PHYSICS | LUND UNIVERSITY

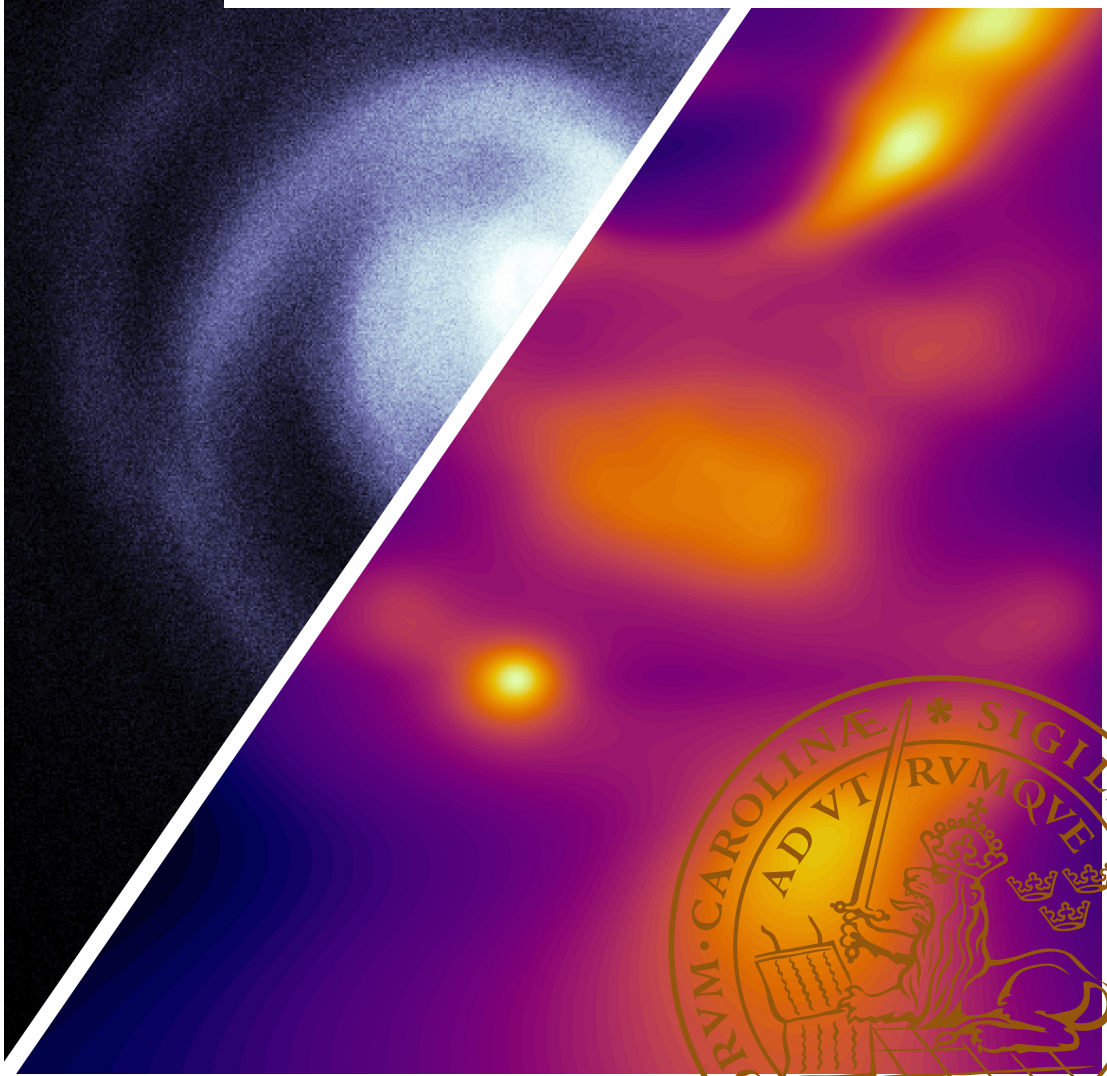

Stellar kinematics in surveys and simulations

Daniel Mikkola

LUND
UNIVERSITY

Thesis for the degree of Doctor of Philosophy

Thesis advisor: Dr. David Hobbs
Co-advisor: Dr. Paul McMillan
Faculty opponent: Dr. Marie Martig

To be presented, with the permission of the Faculty of Science of Lund University, for public criticism in the Lundmark lecture hall (Lundmarksalen) at the Department of Astronomy and Theoretical Physics on the 18th November 2022 at 13:00.

Organization LUND UNIVERSITY Department of Astronomy and Theoretical Physics Box 43, SE-22100 Lund, Sweden Author(s) Daniel Mikkola	**Document name** DOCTORIAL DISSERTATION **Date of issue** 2022-11-18 Sponsoring organization

Title and subtitle
Stellar kinematics in surveys and simulations

Abstract

As the Galaxy evolves it is subjected to a plethora of various dynamical processes that leave their mark upon it. We can view a snapshot of the ongoing processes and connect it to past events. To do this, we require an accurate picture of the stellar motions and positions which are predicted by numerical models. This is the two-pronged approach of Galactic dynamics which connects both theory and observations.

This thesis summarizes three papers where I use this approach to gain new insights into both the current structure of the local Galaxy and one of the processes responsible for it.

In Paper I, I seek to determine the relationship between the vertical extent of stellar orbits and their participation in radial migration across the disc. By numerically simulating different types of discs I am able to determine that radial migration primarily affects stars with small vertical excursions in halo-dominated galaxies and affects all stars more equally in disc-dominated ones.

In Paper II, I utilize the proper-motion limited catalogue of *Gaia* EDR3 to determine the most accurate velocity distribution of white dwarfs to date using a penalized likelihood estimate. This provides kinematics for the stars on the two sides of the bifurcation visible in the white dwarf cooling sequence. The paper is able to find known and some novel structure in the velocity distribution and finds that the bifurcation is related to two separate kinematic populations of white dwarfs.

In Paper III, I further apply the methods of Paper II to two new samples of stars: the local stellar halo and the Solar neighbourhood. With the updated Gaia DR3 I am able to show accurate velocity distributions for both samples and reveal new velocity substructures in the local halo which are part of the *accreted* stellar halo

Key words
Galactic dynamics, stellar kinematics, numerical simulations, statistical methods, solar neighbourhood

Classification system and/or index terms (if any)

Supplementary bibliographical information		**Language** English
ISSN and key title		**ISBN** ISBN: 978-91-8039-411-6 (print) ISBN: 978-91-8039-412-3 (pdf)
Recipient's notes	**Number of pages** 120	Price
	Security classification	

Signature Date 2022-10-05

Stellar kinematics in surveys and simulations

Daniel Mikkola

LUND
UNIVERSITY

Faculty Opponent

Dr. Marie Martig
Astrophysics Research Institute, Liverpool John Moores University,
Liverpool, United Kingdom

Evaluation Committee

Dr. Lise Christensen
Niels Bohr Institute, University of Copenhagen,
Copenhagen, Denmark

Dr. Christa Gall
Niels Bohr Institute, University of Copenhagen,
Copenhagen, Denmark

Dr. Sijing Shen
Institute of Theoretical Astrophysics, University of Oslo,
Oslo, Norway

Front cover: The left side shows one of my simulated N-body galaxies. The right side shows is my estimated velocity distribution for the accreted stellar halo.
Funding information: Computations for this study were performed on equipment funded by a grant from the Royal Physiographic Society in Lund (Stiftelsen Walter Gyllenbergs Fond)

Faculty of Science, Department of Astronomy and Theoretical Physics

ISBN: 978-91-8039-411-6 (print)
ISBN: 978-91-8039-412-3 (pdf)

Printed in Sweden by Media-Tryck, Lund University, Lund 2022

Till morfar

Contents

List of publications

This thesis is based on the following peer-reviewed publications:

I **Radial migration and vertical action in N-body simulations**
Mikkola, D.; McMillan, P. J.; Hobbs, D. (2020)
Monthly Notices of the Royal Astronomical Society, Volume 495, Issue 3, pp. 3295-3306

II **The velocity distribution of white dwarfs in Gaia EDR3**
Mikkola, D.; McMillan, P. J.; Hobbs, D.; Wimarsson, J (2022)
Monthly Notices of the Royal Astronomical Society, Volume 512, Issue 4, pp. 6201-6216

III **New stellar halo substructures from Gaia DR3 proper motions**
Mikkola, D.; McMillan, P. J.; Hobbs, D. (2022)
Submitted to Monthly Notices of the Royal Astronomical Society

Popular summary

Of all things on the celestial vault, the greatest and most striking is the diffuse band of stars that make up the Milky Way, our home Galaxy. To understand how it formed and evolved we need, among other things, a detailed description of how the stars move and where they are located, the field of research called *astrometry*. The first stellar catalogue was created in 200 BCE by Hipparchus in ancient Greece. A little over two millennia later we began measuring stars with space telescopes, the first of which was named *Hipparcos*. This was succeeded by the space telescope *Gaia* which was launched in 2013 and revolutionized the field of astrometry, providing a truly great catalogue of stellar motions and positions. This catalogue has significantly contributed to the research behind this thesis. *Gaia* gives us a very precise picture of how the Milky Way kinematics look today. To complete the picture one also uses numerical simulations to recreate and interpret the features found in observations. The union of theory and observations then reinforce one another and is critical for our understanding of the Milky Way.

The first article in this thesis uses numerical simulations to study how interactions with the Galaxy's spiral arms and bar transport stars radially in the plane of the disc. We find that this migration depends on the Galactic disc's strength and how vertical extended the stellar orbit is. With over 100 simulated discs we could determine that in less massive discs it is mostly the stars close to the disc that migrate and in the opposite case of massive discs they migrate regardless of how far above the disc the orbit goes.

In the second and third articles, we use data from *Gaia*. By using positions and velocities along the celestial sphere, without needing velocities in the line-of-sight direction, we have access to extremely large amounts of data. This way, we obtain an estimate for the local stellar velocity distribution, despite lacking one velocity component. We do this for three samples of data. In the second article, we used white dwarfs, which are the remains of low mass dead stars, and could discover that there were two separate kinematic populations. In the third article, we used the Solar neighbourhood of stars in the disc and a local part of the Galaxy's halo. We were able to identify many known structures in the velocity distribution, as well as some new ones which then belong to the accreted halo, and could be the remains of accreted dwarf galaxies.

Populärvetenskaplig sammanfattning

Utav alla ting på himlavalvet så är det största och mest slående det diffusa band av stjärnor som uppgör Vintergatan, vår hemgalax. För att förstå hur den skapades och utvecklas behöver vi, bland annat, förstå i detalj hur stjärnorna rör sig och var det befinner sig, ett forskningsfält som kallas astrometri. Den första stjärnkatalogen kom 200 f.v.t. från Hipparkos i antika Grekland. Två millennier senare så började vi mäta stjärnor med rymdteleskop, det första då döpt till just Hipparcos. Detta efterföljdes av rymdteleskopet *Gaia* som sattes i omloppsbana 2013 och har revolutionerat astrometrin genom att bidra med en fantastisk stjärnkatalog av positioner och hastigheter. Denna katalog har bidragit stort till forskningen bakom denna avhandling. *Gaia* ger oss en väldigt noggran bild av hur Vintergatans kinematik ser ut idag. För att fullända bilden, använder man sig dessutom utav numeriska simuleringar som kan återskapa och förklara de resultat som vi ser i mätdatan. Föreningen av teori och observationer förstärker då varandra och är kritisk för vår förståelse av Vintergatan.

Den första artikeln i denna avhandling använder just numeriska simuleringar för att studera hur interaktioner med Galaxens spiral armar och centrala stav förflyttar stjärnor radiellt i skivans plan. Vi visar att denna migrering beror på Galaxskivans styrka och hur vertikalt utsträckt stjärnans omloppsbana är. Med över 100 simulerade skivor kunde vi bestämma att i mindre massiva skivor migrerar stjärnor mest nära skivan och i motsatt fall med en massiv skiva migrerar de oavsett hur långt utanför skivan som omloppsbanan går.

I den andra och tredje artikeln använder vi mätdatan från *Gaia*. Genom att vi använder positioner och hastigheter längst med himlavalvet, utan att kräva hastigheter i siktriktningen, får vi tillgång till extremt stora mängder data. Vi kan då uppskatta stjärnornas lokala hastighetsfördelning, trots att vi saknar en hastighet. Detta gjorde vi för tre olika urval av data. I den andra artikeln använder vi vita dvärgar, som är kvarlevorna av mindre massiva döda stjärnor, och kunde upptäcka att där fanns två separata kinematiska populationer. I tredje artikeln använder vi Solens kvarter av stjärnor i skivan och en lokal del av Galaxens halo. Där lyckas vi identifiera många kända strukturer i hastighetsfördelningen, samt några nya som tillhör den ansamlade halon, och skulle kunna vara kvarlevorna av uppslukade dvärggalaxer.

Acknowledgements

I am forever grateful to who is probably my greatest supporter, my beloved partner Tina Sörensen who has been by my side ever since I started my doctoral journey. Your unwavering support has been with me through difficult times with debugging, writing, contemplating, and a global pandemic. I would not be where I am today without you.

My supervisor, David Hobbs. You have mastered the art of knowing when to give a push and when to encourage letting go and taking a step back. You have inspired my work ethic and taken the best care of me as a student of yours. Your door has always been open to me and so has your ear. I will miss walking around the corner to have a chat about just anything.

My co-supervisor, Paul McMillan. Your guidance has been invaluable to me ever since we started working together during my master's project. I am ever impressed by your intuition when looking at new results and to me, you have always been a bottomless fount of knowledge. I regret that this is our last project together, however I think I now know what a good enough scientist would do.

I want to thank the friends I made at Lund Observatory during my stay here. There are too many master students, fellow PhDs, and staff members I want to thank for me to name them all here. Especially I want to thank Eric Andersson whose thesis has been in tandem with mine, which led to good friendship over the years. My first and second office-mates Iryna Kushniruk and Bibiana Prinoth, my closest colleagues in almost all matters besides research. You were the ones I could always 'turn' to and have a chat about either work or life in general. Wherever I end up in the future I am certain I will not have such a great office situation as the one you have given me.

I must not forget to thank the Physics & Lasershow. For almost ten years the show has let me mix work with incredible amounts of fun and given me some of my closest friends. Thank you Per-Olof, Johan Z, Stina, Odd, Johan K, Jonas, Alexandra, Frida, Rebecca, Vassily, Matteus, Lina, David, Elin, and Anna-Maria.

My friends outside of work: Anton, Sara, Fredrik, Marielle, Rasmus, Anna, Jesper, Lovisa, Johan. You have always made sure to keep me humble and to ask me any and all *astrology*-related questions, much to my bemusement. Adrian, I am thankful we reconnected during our PhDs and could share many hours working out or betraying each other in board games.

To conclude, I want to extend my deepest gratitude to the people who made sure I got here today: my family. First, my parents Marita and Seppo, who always made sure to let me explore while providing all the support I needed. My bonus-

mother Suzie, I aspire to have your fortitude. My five brothers: Nicholas, Robert, Christopher, Mattias, and Alexander. Of course also my extra family in Halmstad who have always welcomed me.

Preface

In this thesis, the primary question we seek to understand better is "how do stars move in the Galaxy?". To shed light on this I have examined radial migration in simulated Milky Way-like galaxies to constrain its dependencies. Furthermore, I have estimated the full 3D velocity distributions of different samples of local stars using the largest available astrometric catalogues from the *Gaia* mission. The velocity distributions have allowed us to demonstrate unknown properties of the white dwarf population as well as identify new velocity substructures which can tentatively be linked to accretion events.

This thesis summarises the work which has been published in two papers and is to be submitted in a third. Here follows a brief description of each paper to give the reader an overview of the thesis.

1. *Paper I: Radial migration and vertical action in N-body simulations* - My first paper seeks to determine how effectively stars are radially migrated as a function of how vertically extended their orbit is and how gravitationally dominant their stellar disc is. This was an interesting question since the current understanding of radial migration, following works by Solway et al. (2012); Vera-Ciro et al. (2014, 2016), especially the latter two, had firmly argued for what they call *provenance bias*; radial migration primarily affects stars with small vertical excursions. We investigated whether this *provenance bias* exists regardless of the strength of the spiral arms that cause the radial migration. This had also been investigated in the third of the cited papers, which found that it indeed was. To do this we set up our own simulations with a pure N-body bulge, halo, and disc. We used 11 different set-ups where the halo mass is varied. This allowed the force ratio of halo to disc, $F_{\rm h}/F_{\rm d}$ to vary between 0.5 to 3.2 at a Solar orbit. In other words, we went from strongly disc-dominated systems to halo-dominated systems. We could then quantify the radial migration by comparing the final and initial angular momentum $\Delta L_z = L_{z,f} - L_{z_i}$, and compare it to the vertical action. For a region of the disc, the migration is better described by the spread of ΔL_z, described by its standard deviation $\sigma_{\Delta L_z}$. We looked at the slope of the function that relates the migration efficiency parameter to the vertical action, J_z, at various radii of the disc in all of our simulations. This lets us show that the as the disc becomes more dominant, the slope flattens, and the provenance bias disappears across the whole disc. This was

not the case when migration efficiency was compared to radial action, which implied that there is a difference in the response of migration to increased actions in the various directions. We also recreated the simulations used by Vera-Ciro et al. (2016) and were able to reproduce our results there as well.

2. *Paper II: The velocity distribution of white dwarfs in Gaia EDR3* - In the second paper, the goal is to determine accurate velocity distributions for white dwarfs (WDs) without having to rely on measured line-of-sight velocities. The data releases of *Gaia* have revolutionised the field of astrometry and have produced a truly great catalogue of stellar motions and positions. Already in EDR3, the catalogue contained the full astrometric solution for up to $\sim$1.5 billion sources which completely dwarfs the sample when limited to measured line-of-sight velocities which is about $\sim$7.2 million or about 0.5%. It is typically difficult to get radial velocities for WDs since their spectra have few and broad lines, which means that working with pure proper motions is preferred in order to access a large sample of them. Doing this allows us to use a large sample of 129 675 WDs within 500 pc. Inferring the velocity distribution from proper motions and positions was done for *Hipparcos* data by Dehnen (1998) using a penalised maximum likelihood estimate. The method requires a sample that can be assumed to have proper motions uncorrelated to the on-sky positions. In this case the proper motions in one part of the sky compensate for the missing line-of-sight velocities of another. We applied this method and the related method of Dehnen & Binney (1998) to determine the velocity distributions and velocity dispersions for the WD population. Gaia DR2 had already shown that the WDs have a bifurcation in the colour-magnitude diagram, so the difference between the two sequences was something we chose to investigate. We were able to show that the bluer sequence has lower velocity dispersion, across all magnitudes where the bifurcation exists, than the redder sequence. This means that they comprise two separate kinematic populations. Furthermore, we determined the statistical independence of the two populations with a KS-test. The current best explanation for the bifurcation is atmospheric composition, which would not have a bearing on the kinematics. Our results, therefore, provide support for alternative explanations.

3. *Paper III: New stellar halo substructures from Gaia DR3 proper motions* - The third paper expands the use of the penalised likelihood estimate from Paper II. The benefits of using proper motion catalogues warranted further

exploitation and so we decided to apply the method towards two new samples: the Solar neighbourhood and the local stellar halo. For the Solar neighbourhood, this results in 1 171 846 stars within 200 pc with 10% parallax uncertainty. This sample gives a very accurate view of what the velocity distribution looks like at 'face-value', with all of the most well-known moving groups featuring in the distribution. This also demonstrates that to find additional velocity substructure in the Solar neighbourhood special methods must be applied and in our case, we made use of conditional probabilities of one velocity component of the distribution upon the other. This effectively normalises the distribution along either the rows or the columns of the 2D map and reveals further structure in high-velocity regions. Selecting the local (within 3 kpc distance) stellar halo with a velocity cut of $v_{\rm T} > 200$ km s^{-1} provides us with 456 273 stars. This also reveals the double main sequences which have been previously identified in the colour-magnitude diagram in *Gaia* DR2 Gaia Collaboration et al. (2018b). The sequences are typically associated with a redder 'in-situ' halo and a blue 'accreted' halo which matches well a lower metallicity isochrone. This second sequence has been shown to have significant amounts of accreted substructure (see e.g., Koppelman et al. 2019 and links therein). We create a sample for each sequence with 239 115 and 194 507 stars in left and right sequences respectively. We focus on the accreted population and identify the majority of substructures available in literature. Using the conditional probabilities, we can identify two new features the the accreted halo which have no match in literature: *MMH-1* at $(v_r, v_\phi, v_\theta) \approx (\pm 220, 20, 300)$ km s^{-1} and *MMH-2* at $(v_r, v_\phi, v_\theta) \approx (-20, 180, -100)$ km s^{-1}.

Since the first of the articles is on dynamics in N-body simulations while the second and third are on statistical analysis of astrometric data, the thesis is divided into chapters reflecting this. Chapter 1 gives a structural overview of the Milky Way and explains radial migration. This follows naturally into Chapter 2 which summarises the first article. Chapter 3 gives historical context for the field of astrometry and background for the second and third article's method. Finally, Chapters 4 and 5 summarise the second and third articles respectively.

Chapter 1

The Milky Way as a Galaxy

"I know, it doesn't make any sense, I wish there were sense. Where did all the sense go?"
- Tribore, Final Space

1.1 Components

Throughout history, mankind has sought to understand the night sky and its many features such as stars, clumps, planets or 'wanderers'. But no feature is as large and noticeable as the great spray of stars that make up the Milky Way Galaxy, named so for the milk from Hera's breast in Greek mythology (Leeming, 1998). The suggestion that this milky band of stars was a rotating body that we, the observers, are inside of did not come until Wright (1750). Since then our understanding of our home Galaxy has increased tremendously and we can present stunningly detailed views of it like the map shown in Fig. 1.1. This map is made possible thanks to measurements from *Gaia*'s second data release (Gaia Collaboration et al. 2018a, hereafter DR2). As the figure shows, the Milky Way is composed of several different components with stars differing in spatial distribution, kinematics, chemistry, and age. In the three papers in this thesis, I touch upon almost every component mentioned in Fig. 1.1 and so I will provide a brief description of each one.

1.1.1 Thin disc

The thin disc is what visually makes up the Milky Way and, since it is where the Sun is located, it is the most well-studied of the stellar components. The thin disc is also the site of ongoing star formation which recent estimates place as high as $\sim$3.3 $M_{\odot}yr^{-1}$ (Zari et al., 2022). As the name suggests it is relatively thin

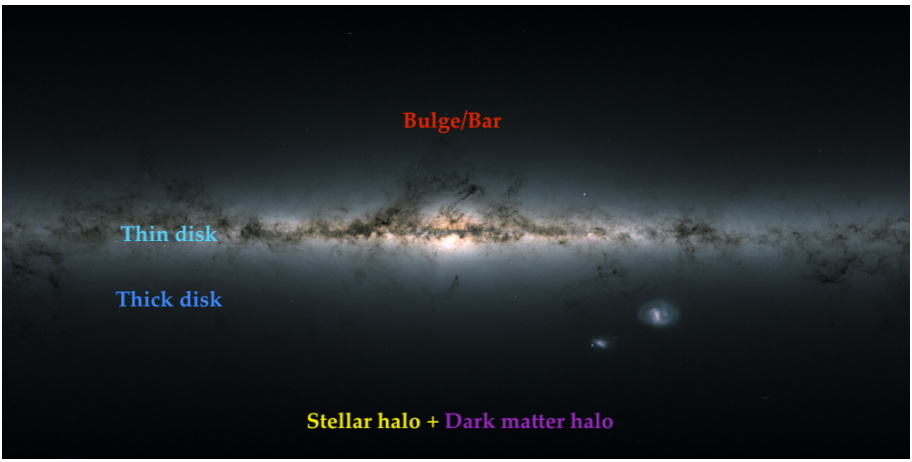

Figure 1.1: All-sky view of the Milky Way Galaxy from Gaia based on measurements of nearly 1.7 billion stars. We mark the location of different components of the Galaxy with different colours. Image adapted from *Gaia* Data processing and Analysis Consortium (DPAC) (CC BY-SA 3.0 IGO).

with a scale length of $R_\mathrm{t} \approx 2.6$ kpc, scale height of $z_\mathrm{t} \approx 300$ pc, and with a mass $M_\mathrm{t} \approx 3.5 \times 10^{10}$ $\mathrm{M}_\odot$ (Bland-Hawthorn & Gerhard, 2016). The thin disc stars are generally young and have abundances of elements produced by the α-process (Burbidge et al., 1957) relative to iron similar to the Sun. These elements have nuclei which are multiples of four, the atomic mass number of the Helium nucleus or α-particle. We measure the relative abundances relative to iron as:

$$[\alpha/\mathrm{Fe}] = \log_{10}\left(\frac{N_\alpha}{N_\mathrm{Fe}}\right)_\mathrm{star} - \log_{10}\left(\frac{N_\alpha}{N_\mathrm{Fe}}\right)_\odot , \tag{1.1}$$

where N is the number of atoms per unit of volume of the respective species.

1.1.2 Thick disc

The second disc of the Galaxy fulfills its name with a scale height of $z_\mathrm{T} \approx 900$ pc, scale length $R_\mathrm{T} \approx 2$ kpc, and mass $M_\mathrm{T} \approx 6$ $\mathrm{M}_\odot$ (Bland-Hawthorn & Gerhard, 2016). Its stars are older (Bensby et al., 2014; Martig et al., 2016) and kinematically hotter than those of the thin disc, since age and velocity dispersion are correlated (Martig et al. 2014; Aumer et al. 2016). In metallicity space, thick disc stars occupy regions of higher $[\alpha/\mathrm{Fe}]$ and are usually linked to the high-α sequence (Katz et al., 2021). How the thick and thin discs formed is still a debated

topic, particularly so the former as explained in Helmi (2020) who also shows that the formation may be related to the evolution of the stellar halo through mergers with nearby galaxies.

1.1.3 Stellar halo

The most extended stellar component is the stellar halo which contains $1.3^{+0.3}_{-0.2} \times 10^9$ $M_\odot$ within $2 < r < 70$ kpc (Mackereth & Bovy, 2020) and is host to the oldest and most metal-poor stars in the Galaxy (e.g., Da Costa et al. 2019; Horta et al. 2022). The orbits of halo stars are less flattened towards the disc and so can be told apart locally by their kinematics. Relative to the discs, the halo stars appear to move with a typical velocity of $\sim$200 km s^{-1}. A commonly used cosmological model is Λ cold dark matter (ΛCDM) which successfully explains, for example, the cosmic microwave background (Planck Collaboration et al., 2020) and the large-scale structure of galaxies (Springel et al., 2005). This theory also explains how stellar halos can form through hierarchical growth with minor and major mergers (White & Rees, 1978; Fall & Efstathiou, 1980). This view matches well with the current understanding of the stellar halo as having an *in situ* component of stars as well as an accreted component that becomes extremely dominant at larger distances from the disc (Naidu et al., 2020). It has also been shown that this accreted component has a plethora of substructures in it attributed to various accreted stellar populations (e.g., Koppelman et al. 2019; Feuillet et al. 2021; Dodd et al. 2022). We will touch more upon this in sections 5.2 and 5.3.

1.1.4 Dark matter halo

There is another halo that is not visible to our telescopes. If we only look at the stellar matter of a galaxy like the Milky Way, the rotational velocity of stars in its outer parts is expected to decrease with distance similarly to Keplerian rotation, in which $v^2_{\rm rot} \propto M/R$. This is not what we observe however, and instead, the rotation curve flattens out which is attributed to the existence of a dark matter halo. Current results place the mass of the dark matter halo at $M_{\rm dh} \approx 1.3 \times 10^{12}$ $M_\odot$ (Posti & Helmi, 2019) and its shape is still a topic of much debate as explained in McMillan (2017). While the debate is ongoing, it is very common in simulations to assume a spherically symmetric halo (e.g., Andersson et al. 2020).

1.1.5 The bulge

In the central regions of the Galaxy lies the bulge, heavily obscured by dust as is clearly visible in Fig. 1.1. The original explanation of the bulge was that of a spherical structure built up through early mergers, which is called a *classical bulge*. This also made sense given the old ages of bulge stars known at the time (Clarkson et al., 2008). More recent results have shown that the bulge has several different metallicity populations (Ness et al., 2013a) including young metal-rich stars (Ness et al., 2014). These younger stars instead suggest that the bulge could have formed through internal disk instabilities. Other works have also shown that parts of the bulge can be formed from the disc through interactions that slowly rearrange energy, angular momentum, and mass, otherwise known as *secular evolution* (Kormendy, 2013). Following star counts in the bulge, it has been established that the majority of bulge stars participate in a *box/peanut*-shaped structure, related to the three-dimensional Galactic bar, with cylindrical rotation (Wegg & Gerhard 2013; Ness et al. 2013b) and Shen et al. (2010) uses the kinematics to constrain its contribution to be less than 8% of the disc mass. In light of these discoveries, it is unclear if the Milky Way even has a classical bulge.

1.2 The bar & spiral arms

Beyond the components mentioned in the previous sections, there are the non-axisymmetric features. In other galaxies they are clearly visible but since we reside inside our Galaxy we struggle to see them as clearly. As an example, we show a simulated galaxy in Fig. 1.2 which has a bar and two spiral arms that can be seen very clearly and represents a typical disc galaxy. Since non-axisymmetric features play an important role in secular evolution we will take a closer look at these features in the Milky Way.

The boxy/peanut-shaped bulge mention in section 1.1.5 is an inner, vertical extension of the Galactic bar (Bland-Hawthorn & Gerhard, 2016). The bulge region reaches to about $\sim$2 kpc (Wegg & Gerhard, 2013) while the bar may reach as far as 5 kpc (Wegg et al., 2015). For this reason, it is sometimes referred to as the 'long' bar. Current estimates for the bar puts its mass at $\sim 1.6 \pm 0.3 \times 10^{10}$ $M_{\odot}$ (Kipper et al., 2020) and using Gaia's third data release (Gaia Collaboration et al. 2022b, hereafter DR3) the bar angle with respect to the Sun-Galactic Centre (GC) is estimated to be $-19.2^{\circ} \pm 1.5^{\circ}$ (Gaia Collaboration et al., 2022a). The bar is not static however and is rotating with a specific angular velocity, called its pattern speed. The pattern speed of the bar is subject to much debate with many

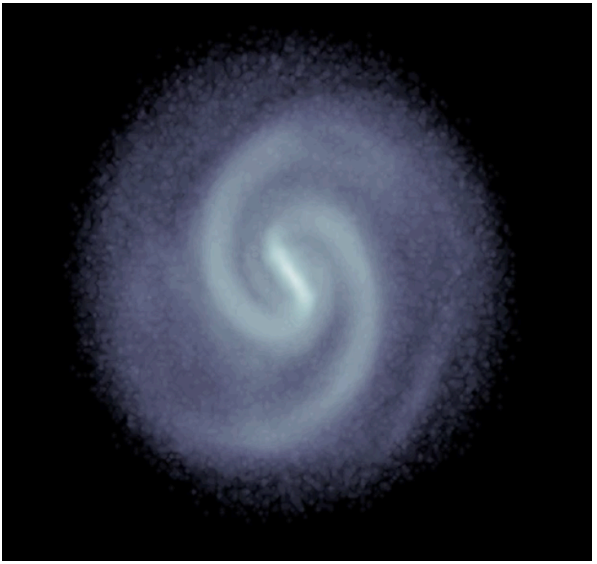

Figure 1.2: An example of a simulated Milky-Way like disc Galaxy with pronounced spiral arms and a central bar.

attempts at determining it. Bland-Hawthorn & Gerhard (2016) review many of the estimates and conclude with an estimated pattern speed of $\Omega_b \simeq 43 \pm 9$ km s^{-1} kpc^{-1}. More recent estimates place the pattern speed of the bar at $\Omega_b = 33.29 \pm 1.81$ km s^{-1} kpc^{-1} (Clarke & Gerhard, 2022) and $\Omega_b = 41 \pm 3$ km s^{-1} kpc^{-1} (Bovy et al., 2019; Sanders et al., 2019), in agreement with the previous value. Pattern speeds of this scale have been called a 'slow' bar scenario.

The other major non-axisymmetric feature of the Milky Way is the spiral arms. They likely wind around the whole disc and as such, we do not have a full picture of them to date and instead must look to whatever parts of them are visible to us from our position as observers in the Galactic plane. Current evidence within the community is that the Milky Way has four approximately symmetric spiral arms (Reid et al., 2019) rather than just two. The names for these four arms as in literature are *Perseus*, *Sagittarius-Carina*, *Scutum-Centaurus*, and *Norma-Outer*. The Sun is believed to lie between *Perseus* and *Sagittarius-Carina* in an inter-arm region. In addition to these arms, very close to the Sun lies the *local arm*, initially believed to be a spur of the *Perseus arm*. It has since been understood to be more similar to the nearby arms with comparable qualities and is perhaps a branch of one of them (Xu et al., 2013). In spiral galaxies, the highest densities of gas and

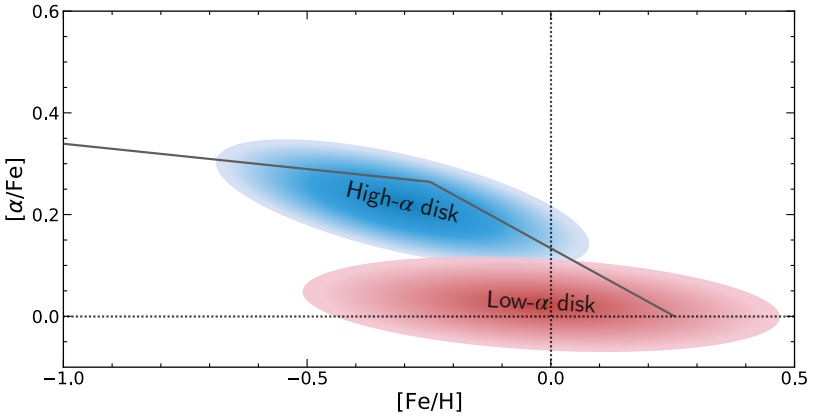

Figure 1.3: An illustration of the distribution of abundance of α-elements vs the abundance of iron. The dotted line shows the location of the Sun and the gray solid line the expected evolution of an isolated region of the ISM.

stars lie along the arms which is the site for most star formation in the disc.

1.3 Radial migration

Since the spiral arms and the Galactic bar are such very prominent features of our Galaxy and in other similar spiral galaxies, it is no surprise that they have a profound impact upon the disc in which they are found and the stars that live therein. One such effect which occurs because of the dynamical interplay between disc and the non-axisymmetric features is *radial migration*, which is the displacement of a star in the radial direction from the Galactic plane. We will soon explain the major processes which cause radial migration but first the importance of radial migration as an ingredient of galaxy evolution, and the evidence to support it, should be discussed.

Let us consider the chemical evolution of the Galactic disc. The abundances of α-elements and Fe over time in an isolated region of the interstellar matter (ISM) are affected by the life and death of its stars through what is called stellar nucleosynthesis (for a review see Edvardsson et al. 1993). In short, stars create elements and enhance the abundances of the next generation. Initially, core-collapse supernovae produce similar amount of α and Fe, but [Fe/H] increases. Eventually, type Ia supernovae begin, which produce Fe but no α-elements and thus in the region [α/Fe] starts to drop. This behaviour produces a trend like the grey line seen in

Fig. 1.3. If we are in a very isolated region, we would expect to see that the stars follow this narrow trend. Neighbouring regions radially inside and outside of the region would however have higher and lower [Fe/H] ranges as it has been shown that [Fe/H] increases radially inwards in the Galaxy (e.g., Hayden et al., 2015). In observations of the Solar neighbourhood (e.g., Edvardsson et al. 1993; Hayden et al. 2015; Bensby et al. 2014) we see a range of different Fe abundances at each [α/Fe], similar to the illustration shown in Fig. 1.3. Similarly, the age-metallicity relationship (AMR) can be expected to follow a narrow line for an isolated region but shows a wide scatter. This can be quite easily explained if the different regions of the disc are not isolated from each other, but rather there is radial mixing between them.

Beyond this rather straightforward example of radial migration, it has been suggested that several other observed features of the Milky Way disc are caused by it. These include the observed bimodality of $[\alpha/Fe]$ in plots like Fig. 1.3 (Schönrich & Binney, 2009; Toyouchi & Chiba, 2016) and the flaring of the outer disc in mono-age populations (Minchev et al., 2012). It is clear that some form of radial migration occurs in the Milky Way and we are today able to estimate the radial displacement of individual stars, such as in Frankel et al. (2018) who find that the Sun has likely migrated from a birth radius of $\sim$5.2 kpc. Therefore it is important to understand the processes by which migration occurs.

1.3.1 Radial heating

One rather simple cause of radial migration is what is called *radial heating*, sometimes called *blurring*. Stars are born in Giant Molecular Clouds (GMCs) which move on nearly circular orbits around the disc. This means that the stars themselves are born on nearly circular orbits. But through the evolution of stellar orbits, they can scatter by interaction with things like other GMCs, clusters, or spiral arms which will lead them onto slightly eccentric orbits, called *epicycle orbits* as they can be described by the *epicycle approximation*. The epicycle refers to the radial and azimuthal oscillations of the perturbed orbit, occurring with an *epicycle frequency*, κ. The reason a perturbed star does not simply move to a different radius when scattered is because of the fine balance between centrifugal and gravitational force keeping it in place. If the star is pushed radially outwards, the centrifugal force decreases faster than gravity and the star moves back in. The star now overshoots to an interior radius where the centrifugal force increases faster than gravity which pushes it back out. In other words, we say that the star is stable to small velocity changes. Because of the oscillations the star will visit different radii than its

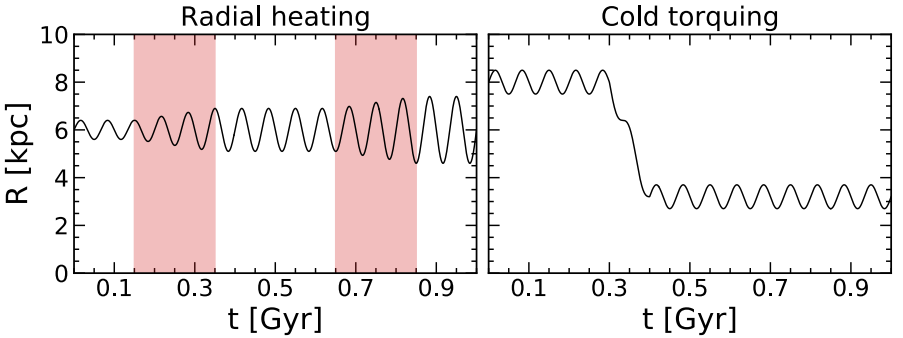

Figure 1.4: A simple sketch of the radial evolution of an orbit that undergoes migration. *Left*: The effect of radial heating or blurring, i.e. the increase of random motion due to dynamical scattering. This process increases or decreases the amplitude of the radial oscillations of the orbit. The shaded regions mark the time during which the radial heating occurs. The average radius, or guiding centre radius, R_g, is never changed during the process. *Right*: The effect of cold torquing or churning by scattering at a corotation resonance, which displaces the guiding centre radius, R_g, but does not increases the amplitude of oscillations and therefore does not increase the radial action, J_R.

original radius, called the *guiding radius*, $R_g = L_z/v_c$, where L_z is the angular momentum perpendicular to the disc and v_c is the circular velocity. It is the process of increasing the amplitude of the oscillations that we call radial heating and we show how this might look in the left panel of 1.4. The scattering process will not change the guiding radius on average but in the cases in which it does, this increases the random motions of the star, including the amplitude of the radial oscillations. In short, while the process of radial heating does not directly relate to a change in guiding radius, such a change can in certain instances also occur.

Given that the stars visit other regions of the Galaxy, they can obviously enrich those regions as well which leads to the conclusion that radial heating can contribute to the width observed in the chemical evolutionary tracks discussed in the previous section. It can, however, be shown, as in Binney (2007), that radial heating will only account for around 50% of the observed scatter in the metallicity and instead there must be some additional source of mixing to explain the measured scatter.

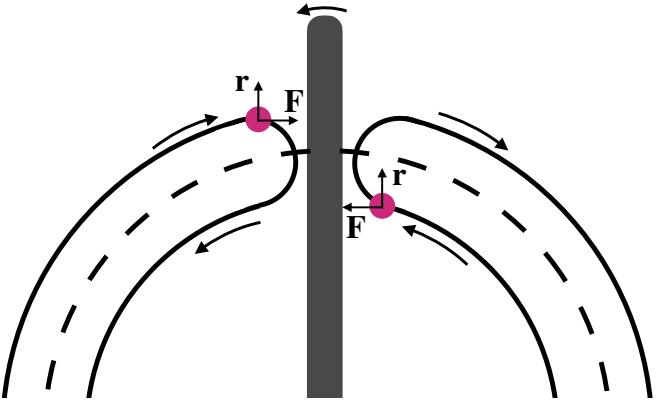

Figure 1.5: The concept of horseshoe orbits and angular momentum transfer near corotation of a non-axisymmetric feature with constant angular speed. The grey bar is a non-axisymmetric feature, with the Galactic centre towards its bottom. The dashed line marks the corotation radius and the pink points are positions along the horseshoe orbit right before angular momentum transfer. The vectors for $\boldsymbol{r}$ and $\boldsymbol{F}$ which gives the torque is indicated

1.3.2 Cold torquing

Another source of radial mixing was described first in a seminal paper by Sellwood & Binney (2002) where it was shown that disc heating is not the dominant effect of the spiral arms. Instead, non-axisymmetric features like the bar and spiral arms can shift the guiding radii of stars without significantly altering their dynamics. This process occurs through resonant interactions with the non-axisymmetric features. The spiral arms or bar will exert a torque that changes the angular momentum of the star's orbit since:

$$\frac{d}{dt}\boldsymbol{L} = \frac{d}{dt}(\boldsymbol{r} \times \boldsymbol{p}) = \boldsymbol{r} \times \boldsymbol{F} = \boldsymbol{\Gamma}. \tag{1.2}$$

Axisymmetric features like bars and spirals move with constant angular velocity, which means that the non-angular velocity increases further out. This means that for stars with approximately constant circular velocity there is a radius at which the velocity of a star and spiral/bar is the same, called *corotation*. Beyond this point, stars move more slowly than the spiral and within it they move faster. Faster stars catch up to the feature and will have a force, $\boldsymbol{F}$, directed towards it. Slower stars instead fall into it with a force in the opposite direction. We illustrate this in Fig. 1.5 which shows that for the fast stars, the torque will be directed inwards, i.e.,

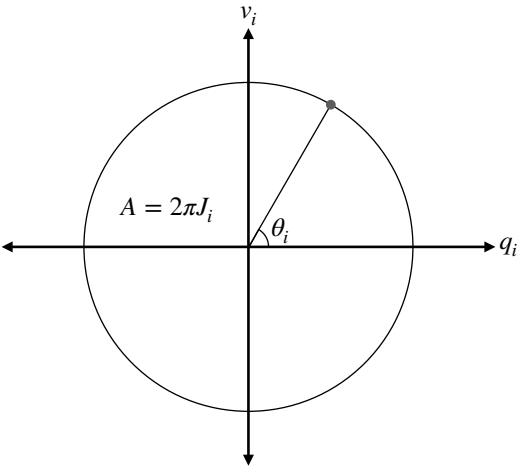

Figure 1.6: A polar coordinate analogy of action-angle variables to phase-space coordinate. An orbit oscillating in some coordinate q_i will have a velocity, v_i which also oscillates. A point on the same orbit can be described with a constant area, $2\pi J_i$, since the action J_i is a conserved quantity, and an angle θ_i.

negative which decreases the angular momentum and transfers it to a smaller R_g orbit where it moves faster. It eventually catches up to the spiral/bar and is given a positive torque, migrating outwards. In this simple view, the orbit would go back and forth but due to the transient nature of spiral arms and the plurality of axisymmetric features, this is not a likely outcome.

This provides the 'torquing' part. The cold part of the term comes from the fact that the migration does not increase the random motion of the affected stars, leaving them kinematically unscathed from the interaction. To properly explain this concept, we introduce *action-angle* variables to describe a stellar orbit. A simple polar-coordinate analogy is given in Fig. 1.6 which shows that an orbit in a certain dimension, i, can be described with two oscillating phase-space coordinates (q_i, v_i) or one constant and one oscillating, (J_i, θ_i). For disc orbits the three actions usually used are: J_r which describes the extent of the radial motion, J_z, the extent of the vertical motion, and J_ϕ which is equivalent to L_z.

If we place ourselves in the rotating frame of a Galaxy, moving with a pattern speed Ω_p relative to the inertial frame, we can describe its total energy or Hamiltonian, E_J, using the Hamiltonian of the inertial frame, E:

$$E_J = E - \Omega_p L, \tag{1.3}$$

Where L is the angular momentum. We call E_J the *Jacobi integral* (see Binney & Tremaine 2008 chapter 3.3.2 for a full derivation) and it is constant in time. So the difference in energy between two points in time is:

$$\Delta E = \Omega_p \Delta L. \tag{1.4}$$

Now we consider the energy separated into a radial and an azimuthal part

$$\Delta E = \frac{\partial H}{\partial L}\Delta L + \frac{\partial H}{\partial J_R}\Delta J_R, \tag{1.5}$$

where J_R is the radial action. If we use Hamilton's equations with $\boldsymbol{J}$ as the momentum and $\boldsymbol{\theta}$ as the coordinate we find:

$$\dot{J}_i = -\frac{\partial H(\boldsymbol{J})}{\partial \theta_i} = 0 \qquad \dot{\theta}_i = \frac{\partial H(\boldsymbol{J})}{\partial J_i} = \Omega_i(\boldsymbol{J}). \tag{1.6}$$

where Ω_i is an angular velocity. This can be understood considering the total energy or Hamiltonian of an orbit is a function of the action, but not of the angle; the energy does not change during an orbit. If the actions, which describe velocities and positions, change then of course so must the energy. We have that $\partial H/\partial J_r = \omega_R$ and $\partial H/\partial L = \Omega$, the radial and azimuthal frequencies. Combining this with eq. (1.5) gives

$$\Delta E = \Omega \Delta L + \omega_R \Delta J_r, \tag{1.7}$$

which when put into eq. (1.4) yields

$$\Delta J_r = \frac{\Omega_p - \Omega}{\omega_R}\Delta L. \tag{1.8}$$

It is the implications of eq. (1.8) that provides the 'cold' part.

Stars have almost constant circular velocity across the disc which means that angular momentum corresponds to guiding radius, (approximately, $L_z \propto R_g$). We know that torquing provides a change in the angular momentum from our discussion above, so this will correspond to a change in the radial action of the orbit unless the angular velocity of the star matches that of the axisymmetric feature, $\Omega = \Omega_p$, which is the case near corotation. This behaviour was demonstrated and detailed in Sellwood & Binney (2002) which showed also that the migration caused by the cold torquing can displace the star on kiloparsec scales, without imparting any increased random motions. The nature of cold torquing is therefore not only impressive but also frustrating since if stars can change their guiding

radius by large scales without having any kinematic evidence of such a process, the history of different regions of the Galaxy becomes much more complex.

As an aside, it is worth mentioning the influence of other resonances that exist besides corotation. A particularly strong such resonance is when the radial frequency, ω_R (identical to κ in the epicyclic approximation), is a multiple of the frequency with which the star encounters the non-axisymmetric feature $(\Omega_p - \Omega)$. In other words when

$$\omega_R = \pm m(\Omega_p - \Omega). \tag{1.9}$$

These resonances are called *Lindblad resonances* after Swedish astronomer Bertil Lindblad (1895 - 1965). The value of m is set by the symmetry of the perturber. For example, $m = 2$ is a two-armed spiral or bar and $m = 4$ is a four-armed spiral. The positive sign corresponds to an orbit in which the rotating feature sweeps by the slower star as it completes m radial oscillations and is known as an *Outer Lindblad Resonances* (OLR). The negative sign is when the fast star rotates past the rotating feature by the time it completes its m radial oscillations and is then called an *Inner Lindblad Resonance* (ILR). At these resonances, we have from eq. (1.8)

$$\Delta J_r = \pm \frac{1}{m} \Delta L, \tag{1.10}$$

which shows how migration at these resonances increases the radial action, therefore making them a potential source of migration by radial heating as discussed previously.

Clearly, we must understand how stars are radially migrated. In particular, the process of cold torquing must be well understood since it is unique in the fact that it leaves no dynamical trace. Without these insights we cannot have a full picture of the history and evolution of our Galaxy.

Chapter 2

Paper I

2.1 Introduction

In my first paper, the aim is to establish the relationship between the efficiency of radial migration by cold torquing and the vertical action of stars. We seek to answer the question: do stars with large vertically extended obits migrate equally, or less efficiently, than those with smaller vertical extensions? Radial migration is a complicated process which can not be accurately described with an analytical expression. It is also a process which occurs over hundreds of millions of years, so we cannot observe it directly. For these reasons, we make use of numerical or 'N-body' simulations. In addition, using isolated disc galaxy simulations lets us have a great deal of control over the parameter space.

The paper particularly focuses on determining the efficiency of radial migration as a function of the kinematics of their orbits. This is not a topic that has gone entirely without study, of course. The efficiency of radial migration as a function of radial velocity dispersion is investigated in Solway et al. (2012), Vera-Ciro et al. (2014), and Daniel & Wyse (2018) who all agree that migration is reduced with increased radial motion. A similar trend can be seen when investigating vertical motion or vertical scale height. This is studied by several articles including Solway et al. (2012); Vera-Ciro et al. (2014); Halle et al. (2015); Vera-Ciro et al. (2016) and the conclusion is the same: radial migration is reduced with increased vertical excursion measured either through scale height or velocity dispersion. This is dubbed the *provenance bias* by Vera-Ciro et al. (2014). However, Solway et al. (2012) found that this effect was rather minor and was even used by Schönrich & McMillan (2017) as justification for migration to be independent of actions in

their model. They also speculate on the difference between the works of Solway et al. (2012) and Vera-Ciro et al. (2014) being due to the strength and morphology of the spiral arms.

The idea of a provenance bias can be understood by considering the interaction between a star and a spiral arm. Cold, circular orbits will spend more time near the corotation resonance of the spiral and be more prone to migration. However, a sufficiently strong spiral arm from a massive stellar disc could perhaps be strong enough to migrate stars that reach larger vertical excursions as well. In Vera-Ciro et al. (2016) they create three different simulations of live discs in static dark matter halo potentials. These go from a lighter disc to a heavier disc, with the heavier disc resulting in fewer, stronger, spirals (D'Onghia, 2015). They claim that the provenance bias is present regardless of morphology which does not provide an explanation for the result of Solway et al. (2012).

In the paper, we seek to answer how this provenance bias is affected by spiral morphology and disc dominance. To do this, we generate a large number of N-body simulations where the ratio of the halo to disc strength is varied to produce discs with different strengths and morphology. We investigate the radial migration that occurs in these simulations and quantify it as a function of disc dominance. Specifically, we quantify the provenance bias of the migration. We determine that the slope of radial migration efficiency as a function of vertical action is itself a function of the dominance of the disc. The slope is steep for weaker discs (i.e., a provenance bias exists) and flattens for stronger discs, supporting the idea that strong spirals can migrate stars on vertically extended orbits. For radial action, we find that there is a provenance bias regardless of disc dominance.

2.2 Setting up simulations

All of our simulations are set up and run using packages available as part of the NEMO[1] (Teuben, 1995) toolbox. We start with a pure N-body isolated galaxy system designed to be similar to the Milky Way. The scale lengths and masses of components we use are chosen with inspiration from McMillan (2017). The full specifics of each component and the chosen parameters are found in paper I.

We follow the procedure of McMillan & Dehnen (2007) which describes the production of an equilibrium system of bulge, halo, and disc. The paper describes the procedure used in the NEMO package MKGALAXY, which in turn uses MKWD99DISC and MKHALO to create the different components. This disc has a

[1] `https://teuben.github.io/nemo/`

standard shape with a density profile that decreases exponentially in radius and has a sech^2 vertical profile:

$$\rho_{\rm disc}(R,z) = \frac{1}{2z_{\rm d}}\Sigma_0 \exp\left(-\frac{R}{R_{\rm d}}\right) {\rm sech}^2\left(\frac{z}{z_{\rm d}}\right). \tag{2.1}$$

The dark matter halo and bulge are both designed to have a spherical density distribution:

$$\rho(r) = \frac{\rho_0}{x_i^{\gamma}(x^{\eta}+1)^{(\gamma_o-\gamma_i)/\eta}} {\rm sech}\left(\frac{r}{r_t}\right), \tag{2.2}$$

with the parameters chosen for the halo to provide a Dehnen-McLaughlin profile (Dehnen & McLaughlin, 2005) which has the advantage of being fully analytic with a smooth transition between inner and outer parts of the distribution. It also matches very well to simulated dark matter halos. The bulge uses a standard Hernquist profile (Hernquist, 1990).

Starting from these initial conditions we change only the mass of the dark matter halo. We create eleven different setups with halo masses ranging from 1.7×10^{11} M$_\odot$ to 1.02×10^{12} M$_\odot$ which corresponds to the ratio of the radial force from the halo to the disc, $F_{\rm h}/F_{\rm d}$, ranging from around 0.5 to 3.2 at $R = 8$ kpc and $z = 0$. In other words, we go from disc-dominated systems to halo-dominated systems. Each dark matter halo setup is also generated with ten different random seeds to estimate stochasticity, resulting in a total of 110 simulations.

2.3 Evolution of non-axisymmetric features

To capture the evolution of the simulated galaxies and their spiral arms and bars we use two approaches. The first is a direct visual inspection of the disc morphology in the plane of rotation at three different times, which correspond to 'early', 'evolved', and 'late' times or 0.3 Gyr, 1 Gyr, and 4 Gyr respectively. This is shown in Fig. 2.1. Since we are in a pure N-body simulation, we do not get much secular evolution beyond this time as the disk kinematics become too heated to participate in the dynamical interactions with the spiral arms. For this analysis we also only look at the lightest halo, 1.7×10^{11} M$_\odot$; the heaviest halo, 1.02×10^{12} M$_\odot$; and the one in between, 5.1×10^{11} M$_\odot$ as representative cases. This gives a disc-dominated case, a halo-dominated case, and something in between.

These simulations highlight that a very halo-dominated system leads to many, weaker arms rather than grand-design spirals and is unable to form a bar as well. In contrast to this, the disc-dominated system shows impressive arms, a bar, as

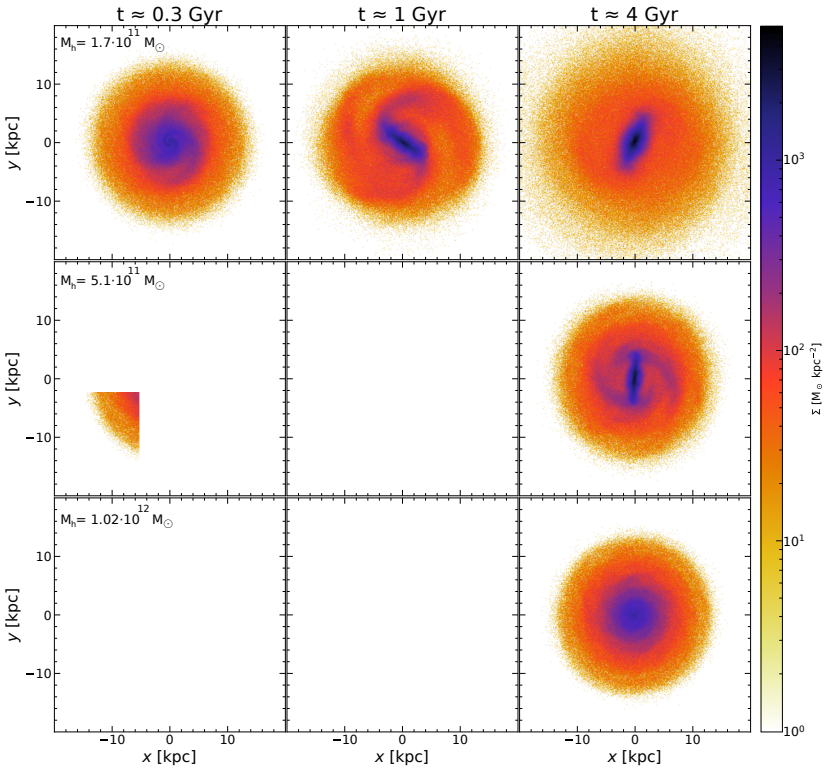

Figure 2.1: Three simulated galaxies seen face-on with masses: 1.02×10^{12} $M_\odot$, 5.1×10^{11} $M_\odot$, 1.02×10^{12} $M_\odot$ in each row. The time of the snapshots for each column is indicated on the top. The different evolution of non-axisymmetric features is seen.

well as the heating mentioned before as the disc becomes extended by comparison to its quiescent counterparts.

The second approach is using a Fourier analysis to extract the power spectrum of different modes, m, or number of spiral arms ($m = 2$ is a two-armed spiral or bar). This method is described thoroughly in Roškar et al. (2012) and our paper. This analysis further strengthens what is already discussed above. The disc-dominated system sees a strong $m = 2$ resonance arise already at around 0.3 Gyr, probably a mixture between the spirals and bar. It has a pattern speed of $\sim$30 km s^{-1} kpc^{-1}, comparable to that of the Milky Way bar. The intermediate disc takes until after 2 Gyr to form a $m = 2$ feature with weaker multi-arm features prior to this time. Finally, the halo-dominated system barely sees any significant modes

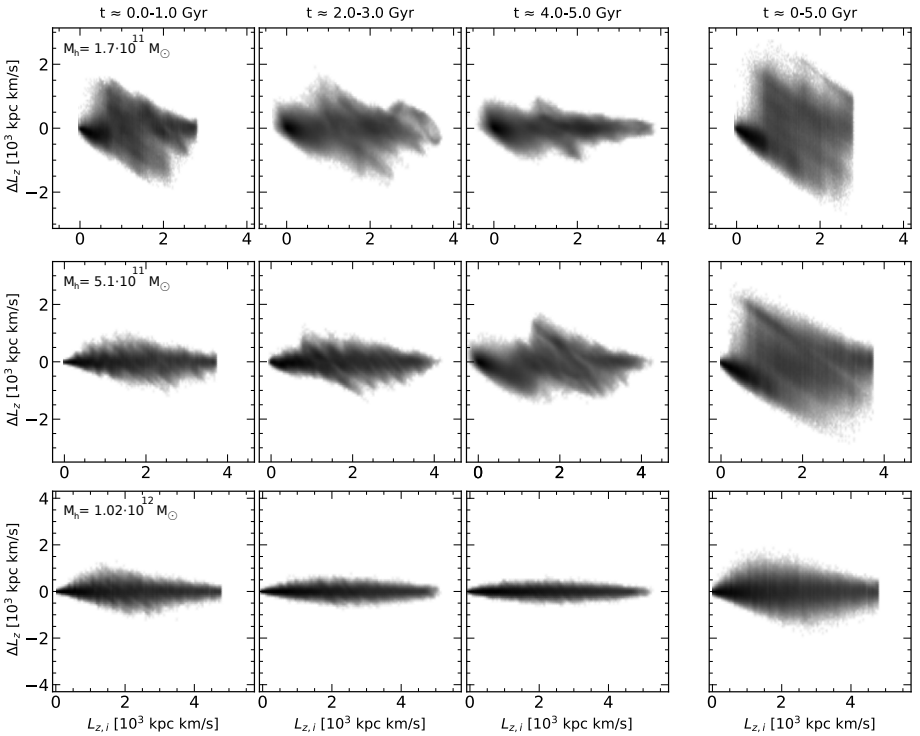

Figure 2.2: Change in angular momentum, ΔL_z, between two points in time as a function of initial angular momentum, $L_{z,\mathrm{i}}$. The rows correspond to the same simulations as in Fig. 2.1 and the time of angular momentum change is shown at the top. The amount of angular momentum change in each case is closely related to the evolution of strong non-axisymmetric features in the simulation.

appear apart from a very weak $m = 6$ feature briefly around 0.2 Gyr. Our results agree with D'Onghia (2015) that the disc-dominated systems form fewer, stronger spirals. This, of course, has implications for radial migration.

2.4 Quantifying radial migration

To gauge the amount of radial migration that occurs across the disc, we use a common approach of looking at the change in angular momentum, $\Delta L_z = L_z(t_2) - L_z(t_1)$, between two points in time t_1 and t_2. This can be compared against the initial angular momentum of the particles, $L_{z,\mathrm{i}}$, which is a proxy for the guiding radius. This is seen in 2.2 for the three simulations mentioned in sec-

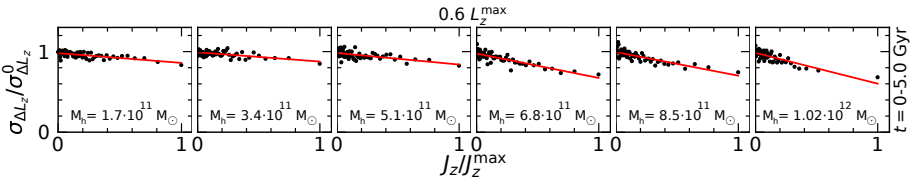

Figure 2.3: Change in angular momentum, ΔL_z, between two points in time as a function of initial angular momentum, $L_{z,\mathrm{i}}$. The rows correspond to the same simulations as in Fig. 2.1 and the time of angular momentum change is shown at the top. The amount of angular momentum change in each case is closely related to the evolution of strong non-axisymmetric features in the simulation.

tion 2.3 and shows how the strength of the secular features affects the migration. Note that diagonal features in this space corresponds to migration across a corotation resonance since particles interior to the resonance are migrated outwards, gaining a positive ΔL_z and vice-versa for the particles exterior. For example, consider the intermediate case. As was shown in the previous section, the bar forms not until after 2 Gyrs to form its largest $m = 2$ mode. We can see here that the most significant migration does not transpire until after this. We also see that the disc-dominated system has strong early migration which calms down as the disc has become heated. Since we have quantified the amount of migration as a function of angular momentum and shown how it relates to the disc morphology, we are equipped to tackle the primary question, the provenance bias.

We want to see how the migration changes as a function of the vertical action J_z across the disc. The particles are therefore binned 100x100 in the space of initial vertical action, $J_{z,\mathrm{i}}$, and initial angular momentum, $L_{z,\mathrm{i}}$. In each of these bins, the amount of migration occurring is quantified by the dispersion of angular momentum changes, $\sigma_{\Delta L_z}$, which we call the radial migration *efficiency*. We can then separate different bins in $L_{z,\mathrm{i}}$ into separate cases and investigate the behaviour of migration efficiency $\sigma_{\Delta L_z}$ as a function of initial vertical action $J_{z,\mathrm{i}}$. In the paper we use three values of $L_{z,\mathrm{i}}$ as representative of separate radial disc regions: 0.4, 0.6, and 0.8 of the maximum $L_{z,\mathrm{i}}$, corresponding to about 15 kpc. In this overview, we will show the $0.6L_z^{\max}$ case only. There are also inconsistencies between the simulations and in radius that require special attention. At smaller guiding radius particles reach much larger extents in vertical action due to the gravitational potential. To correct for this J_z is normalized such that it ranges from 0 to 1 with 1 corresponding to the largest extent in J_z. We also know that total migration is less in the halo-dominated simulations (as seen in Fig. 2.2). We

wish to know how migration is biased to higher vertical actions, rather than how much migration occurs in total, and so we also normalize $\sigma_{\Delta L_z}$ by dividing it by its value at $J_z = 0$ km s^{-1} kpc^{-1}. The result as seen in Fig. 2.3 allows us to determine the slope in this space, which is a measure of the provenance bias. A flat slope means that migration is equally efficient at all values of J_z and a strong negative slope means that migration preferentially affects low J_z particles.

This result shows that the provenance bias is a function of the disc dominance of the simulated system. We see the same trend in the slopes at the two other angular momentum slices considered, $0.4L_z^{\max}$ and $0.8L_z^{\max}$. We compare our results with Vera-Ciro et al. (2016) by reproducing their Milky Way-like simulation and altering the disc dominance through the disc mass. We then apply our analysis approach to these simulations and quantify the migration in the same way as for our own simulations. This leads us to the same conclusion as above: the slope of migration efficiency flattens with disc dominance. The fact that we see this and they do not is likely because of the lengths we go to in order to quantify the migration. We also investigate the radial bias of migration efficiency to find that there is a provenance bias that is independent of disc dominance, suggesting different responses to cold torquing efficiency with increased action in the disc plane instead of orthogonal to it.

These results have significant implications for galaxy evolution. If stars on vertically extended orbits, which are typically older, can be migrated then any interpretation of stellar distributions as a function of age is contaminated. The results also provide necessary constraints for analytical modelling of radial migration, which is a necessary part of any analytical galaxy evolution model.

Chapter 3

Motions of stars

"The stars are far brighter, Than gems without measure."
- J. R. R. Tolkien, The Hobbit

3.1 The oldest science

The fascination of mankind with the celestial sphere has undoubtedly been around for far longer than historical records can demonstrate. Beyond a scientific curiosity, the night sky has had practical purposes that have been used throughout history. Polaris points the way north for travellers of all sorts. The blurring of stars can tell sailors that it is windy at sea. Agriculture heavily relies on the use of calendars based around the Sun and Moon. The relationship between astronomy and humans was arguably more tangible and transparent in the past than it is today when non-astronomers do not need to think about these matters very often.

In the last few decades, the study of prehistoric astronomy has boomed into its own field called archaeoastronomy and revolves around the study of prehistoric sites and their possible astronomical association (see Magli 2020 for a review). These sites have origins dating back several millennia BCE. The earliest historically verified accounts of astronomy come from Mesopotamia and the ancient kingdoms of Sumer, Assyria, and Babylonia. From this region have been found clay tablets noting down positions and locations for constellations and planets. One significant example of such is the *Mul-Apin* clay tablet, shown in Fig. 3.1, which dates back to a little over 1000 BCE (de Jong, 2007).

Around 200 BCE the first star catalogue was made by *Hipparchus* in ancient

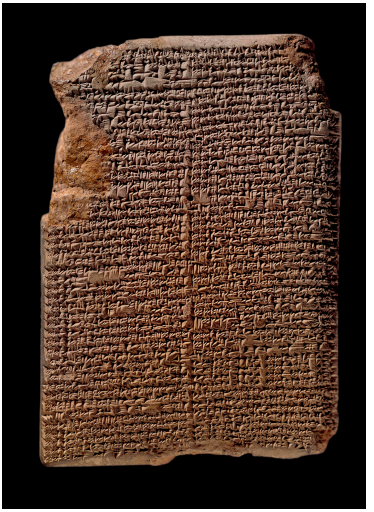

Figure 3.1: The Mul-Apin clay tablet, tablet 1. The tablet has sections locating constellations in relation to each other and lists stars and constellations according to celestial latitude among other entries.

Greece[1]. This catalogue contained positions of stars and is often linked to the birth of *astrometry* as a subject, the study of positions and movements of celestial bodies with precise measurements. As the Roman empire fell and the Dark Ages began, astrometric advances were made to wait. In 1428 a 36-meter sextant was constructed in Uzbekistan by the grandson of the Mongol conqueror Tamarkand, *Ulugh Beg*. This provided a new star catalogue of 994 stellar positions accurate to a degree. The next advancement came from Scandinavia as *Tycho Brahe* (1546-1601) on the Danish island of Hven, using a quadrant of around seven meters at his Uraniborg observatory, measured a thousand stellar positions. His accuracy reached about $20''$. In order to perfect the art of navigation, it was necessary to determine the longitude of various places. For this purpose, the Royal Greenwich Observatory was founded in 1675 and its first Astronomer Royal was *John Flamsteed* (1646-1719), tasked with determining the motions of the heavens. After his passing was published a catalogue of 2935 stellar positions accurate to $10''$-$20''$, the *Historia Coelestis Brittanica* (Flamsteed, 1725), the first catalogue using

[1] The history of astrometry is described in much greater detail in Perryman (2012) than it is here and we encouraged the interested reader to have a look.

a telescope. This expanded rapidly thereafter and had reached 50 000 stars with $3''$accuracy in *Histoire Céleste Française* by *Jérôme Lalande* (1732 - 1807) (de Lalande, 1801).

The next step is not an increasingly large catalogue. Instead, through separate works by *Wilhelm Struve* (1793-1864), *Friedrich Bessel* (1784-1846), and *Thomas Henderson* (1798-1844) the first stellar parallaxes (ϖ) were published between 1837 to 1839. The parallax is the apparent angular displacement of an object due to the displacement of the observer. When driving down a highway, you will notice that as you move, the mountains in the background move more slowly across your field of vision than the trees by the side of the road. This angular displacement is the parallax, larger for nearby objects, and smaller for more distant ones. The same can be done for the stars, as the closer a star is the more it is displaced across the celestial sphere as the Earth orbits the Sun. The distance to stars based on their apparent motions could now be measured, albeit for individual stars at first. It is worth noting the scale of these distances. Bessel's measurement of 61 Cygni's parallax was $0.314''$, corresponding to $\sim$3 pc or roughly 90 trillion kilometres. The enormity of the Universe could no longer be questioned. During the next century and a half, the number of available ground-based parallax measurements grows rapidly and culminates in 1995, when the *Yale Trigonometric parallax Catalogue* is published by *William van Altena* (van Altena et al., 1995). The parallax measurements are then limited to an accuracy of $0.5''$ due to the flickering of the Earth's atmosphere which is reduced to $0.01''$ when averaging over many measurements. One workaround is adaptive optics, distorting the mirror to compensate for the atmosphere, which is used in the GRAVITY instrument (Eisenhauer et al., 2011) to achieve up to $0.003''$. Even then however, the entire sky cannot be covered. Furthermore, it is not the most precise astrometry we can get. Further precision requires that the next advancements be made using space telescopes.

3.2 Hipparcos & Gaia

In 1989, following a little over two millennia of astrometric catalogues, the first astrometric satellite was launched by ESA with the name *Hipparcos*, named after the author of the first catalogue. Eight years later the catalogue was published in Perryman et al. (1997), containing positions, proper motions (the on-sky angular motions), and distances for 117 955 stars, accurate to a milliarcsecond (mas). This mission was also used to produce the lower-precision Tycho catalogue (named for Tycho Brahe), which expanded the number of stars with proper motions and

positions to 2.5 million (Høg et al., 2000). The scientific gifts of Hipparcos were many, and the achievements made possible are reviewed in Perryman (2009).

The opportunities awarded to astronomers by Hipparcos perhaps left the community hungry for more because not long after, in 2013, its successor was launched and was designed to provide the single largest improvement on past available astrometry, by a wide margin. This mission is called *Gaia* (Gaia Collaboration et al., 2016a) and currently provides the largest available set of astrometric data.

The Gaia mission has so far had three full data releases (DRs). DR1 (Gaia Collaboration et al., 2016b) released with the five-parameter astrometric solution (positions, parallax, proper motions) for 2 million sources. The total number of sources was closer to 1.1 billion, but getting the astrometric solution using one year's worth of data required the adoption of the *Tycho-Gaia Astrometric Solution*, described in Michalik et al. (2015). Two years later DR2 (Gaia Collaboration et al., 2018a) released with $\sim$1.3 billion five-parameter sources. Not only that, but the onboard spectrometer provided $\sim$7.2 million radial velocities, completing the full 6D phase-space information for these stars in addition to 3D position with on-sky velocities. Two years later again, the Early Data Release 3 (Gaia Collaboration et al., 2021) arrived with five-parameter solutions for $\sim$1.4 billion sources. The radial velocities came with DR3 (Gaia Collaboration et al., 2022b) and we now have $\sim$33 million sources with RVs. The precision of Gaia is of course also a massive improvement on that of previous catalogues. From brightest to faintest sources, Gaia now has an uncertainty of 0.01-1 mas in position, and 0.02-1.3 mas in parallax, 0.02-1.4 mas yr^{-1} in proper motion. The astrometry of the faintest stars is about as accurate as Hipparcos could provide for any star, and the ratio of sources in Hipparcos to those in Gaia is about $8 \times 10^{-5} : 1$, representing an increase of about 12 000 times.

In addition to astrometry and spectroscopy, Gaia also provides photometry, variable sources, as well as some parameters for Solar system objects[2]. Gaia is not done quite yet and the future is sure to be exciting with a successor mission being planned which would conduct astrometry in the infrared (Hobbs et al., 2021). It does not seem like the exponential growth of astrometry is stopping anytime soon, much to the benefit of our understanding of the universe.

For everything Gaia does well, we need to discuss a shortcoming of the data with respect to studying Galactic dynamics that is central to the work in Papers II and III. Radial velocities were not available in the Gaia catalogue until DR2, and

[2]For a more exhaustive list of everything in the data releases, see the 'info' section of each release on `https://www.cosmos.esa.int/web/gaia/data`

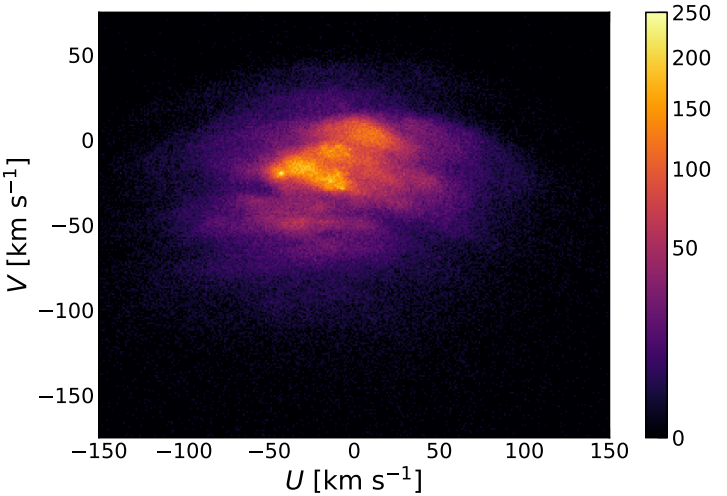

Figure 3.2: The number density distribution of sources from DR3 with radial velocities in the Solar neighbourhood. There is clearly a great deal of structure present already in close proximity to the Sun. The colour scale shows $\sqrt{N}$ and the axes show Galactic velocities U, towards the Galactic centres, and V, in the direction of Galactic rotation.

when released was only available for about 0.5% of the astrometric solutions. This was slightly improved with DR3, which reached closer to 2%. This still leaves the vast majority of the data without 6D phase-space information. Full phase-space information is important because, as Dehnen (1998) puts it, "*The dynamical state of a stellar system is completely described by its phase-space distribution function* $F(\boldsymbol{x}, \boldsymbol{v})$*"*. Practically we cannot determine the full distribution in a realistic way and instead, we seek to determine more local variations of the velocity distribution $f(\boldsymbol{v})$.

Now comes the issue; we do not have 3D velocities for the majority of these sources. How can we hope to determine the velocity distribution? To begin with, we can simply work with the sources that have radial velocities. This has been done of course and for DR2 it was in one of the demonstration papers, (Gaia Collaboration et al., 2018c). We use DR3 to recreate the same plot here, using a similar Solar neighbourhood sample we have around 500 000 stars, whereas in DR2 the sample contained ∼350 000 stars. The velocity distribution can be seen in Fig. 3.2. This figure shows us that the velocity structure of the Galaxy, even locally, is anything but straightforward. Structure in velocity space can be

caused by a variety of processes (see, e.g., Antoja et al., 2010). Originally it was thought to come from disrupted stellar clusters. Newer suggestions have been accreted dwarf galaxies and close passings by external galaxies. Last but not least, the resonances of the spiral arms and bar, as discussed in the context of Paper I, can cause substructure in velocity space as well. We can with ease understand how decoding the velocity structure of the Galaxy will provide valuable insight into its evolution and history. It is therefore vital that we have access to as many stars as possible.

So what about the remainder of the sources? It turns out that all hope is not lost. Already in Dehnen (1998) the velocity distribution from Hipparcos was determined, despite the lack of radial velocities, by employing a clever approximation of a velocity distribution which is isotropic across the sky and then inferring $f(\boldsymbol{v})$ with a penalized maximum likelihood estimate (MPLE) (we will return to this in section 4.3). Similarly the average velocities and the velocity dispersion were determined in Dehnen & Binney (1998). Other studies that work around the absence of measured radial velocities include Antoja et al. (2017) with estimates of disc velocity asymmetries, Koppelman & Helmi (2021) who determined the Milky Way's escape velocity, and McMillan et al. (2022) who looked to the outer parts of the disc near the anti-centre and showed that the velocities exhibit properties that match well with being perturbed by a dwarf galaxy. At least for now, it is necessary to use proper motion-limited samples if we wish to have access to catalogues that span a greater part of our Galaxy, and if we wish to have access to all kinds of stars.

The astrometric renaissance is now and it is an exciting time for all fields of astronomy that can make use of the impressive data that is not only currently released but is sure to arrive in the foreseeable future.

Chapter 4

Paper II

4.1 Introduction

In Paper II we deal with the velocity distribution of local stars which was discussed in the previous chapter. Specifically, we determine the velocity distribution and velocity moments of Solar neighbourhood white dwarfs (WDs) in Gaia EDR3. In order to do this, we make use of the methods derived in Dehnen (1998) and Dehnen & Binney (1998) the first of which has not been employed for the *Gaia* data prior. Since the method does not rely on any measurements of radial velocity the WDs are ideal candidates since they very rarely have such measurements available.

The velocity distribution is a powerful tool to decode the evolution of the Milky Way's components, as the community has been able to show in the past few decades. Recent research has been able to show a staggering amount of substructure in the velocity distributions (Antoja et al., 2012; Kushniruk et al., 2017; Gaia Collaboration et al., 2018c) where we can see individual velocity structures up to hundreds of km s^{-1} away from Solar motion as well as horizontal arches in (U, V) that span across the distribution. In addition to classical motions in U, V, W, the field has grown to include distributions in actions and angles, called orbit space (e.g., Trick et al. 2019, 2021; Trick 2022). In orbit space, we can see clear ridges that are linked closely to the various structures in velocity space. Going forwards, both of these spaces will be important to understand the dynamical structure of the Milky Way.

The velocity distribution of WDs has, as mentioned, not been as easy to probe as that of the rest of the stars in the Solar neighbourhood. This leads to smaller

samples which a couple of decades ago were only in the few hundreds (Sion & Liebert, 1977; Sion et al., 1988) and more recently samples which range from a couple of thousand to a few tens of thousands (Rowell & Hambly, 2011; Anguiano et al., 2017). Recent works that investigate the kinematics of WDs are Torres et al. (2019) who used Gaia to identify the *Hercules* stream in the WDs and Raddi et al. (2022) who determined the age-velocity dispersion relation of WDs. These samples are about as large as any that have been used, with $\sim$14 000 and $\sim$3000 for the two papers respectively. In my second paper, our method provides us with a sample of 129 675 WDs, the largest to date. We use this sample to identify known substructures as well as some novel features in velocity space. In addition to this, we also manage to identify two kinematically separate WD populations, which are attributed to two parallel cooling sequences seen in the colour-magnitude diagram (CMD) of WDs and demonstrated in section 4.2. We tentatively linked this to recent star formation which, it has been suggested, matches the times of flybys of nearby dwarf galaxies (Ruiz-Lara et al., 2020).

4.2 White dwarfs

Stars can be called 'nuclear foundries', as they fuse hydrogen into helium, 'shaping' metals from other metals through nuclear processes. This process creates outward thermal pressure which holds the star up against gravitational pressure in hydrostatic equilibrium. The hydrogen is not infinite and eventually runs out and the star contracts, shedding its outer layers while the core begins fusing helium into heavier elements, creating a planetary nebula around it. For massive stars, the core is large enough that many heavier elements can start fusing but for stars between about $0.6 - 10$ $M_\odot$, at some point this is insufficient and 'electron degeneracy'[1] occurs and provides the necessary outward pressure. The star no longer fuses and all that is left is the core, a stellar 'corpse' called a white dwarf. This is the fate of 97% of all stars in the Milky Way (Fontaine et al., 2001). The WD will live for a long time, but cools slowly, growing fainter and redder over time which can be seen in the CMD of WDs, shown in Fig. 4.1. The WD will be difficult to observe photometrically, as it is rather faint, and spectroscopically, due to the metals sinking below the observable photosphere as well as thermal broadening.

Despite this, Gaia is able to observe quite a large number of WDs photometrically. In the Solar Neighbourhood (within 500 pc) we can, after some quality cuts, find about 130 000 WDs in EDR3. However, if we use an even closer sample

[1] Electron degeneracy pressure and more is explained in Kippenhahn et al. (2012)

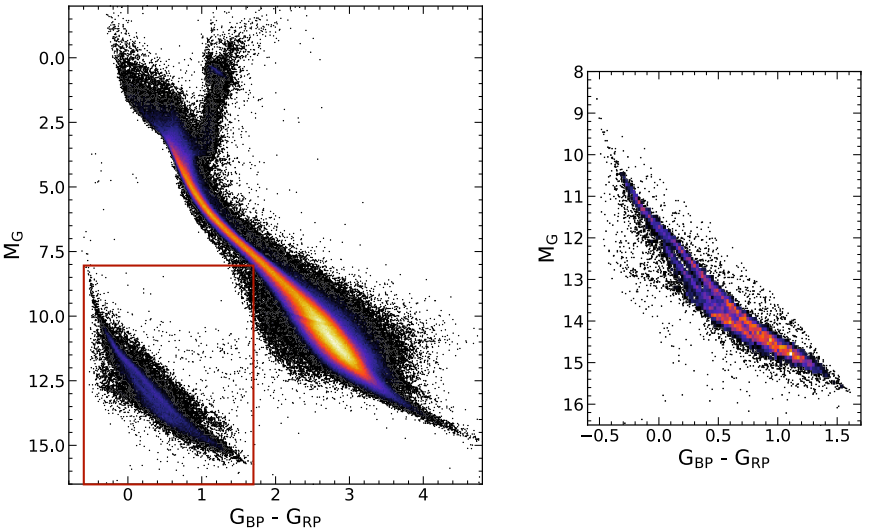

Figure 4.1: Colour-magnitude diagram of stars available as part of the Gaia data. The colour shows the square root of the number density. The left panel shows all stars in DR3 that are within 200 pc overlaid with a 500x500 histogram. The red box shows the WD region which is then shown on the right in a similar style but for stars within 100pc and with increased bin width. A separation into two sequences can clearly be seen.

limited to 100 pc, we can observe that the WD sequence is in fact not singular, but split into two. This result was first identified in Gaia Collaboration et al. (2018b) and has had two major suggestions put forth to explain it. Explanation **a)** suggests that the second sequence arises due to atmospheric differences in WDs. The upper, redder, sequence have hydrogen-dominated spectra (called DAs and constitutes ∼80% of observed WDs) whereas the lower, bluer, sequence contains WDs with Helium (called DBs) or heavier elements dominating their atmospheres. We can refer to this simply as DAs or non-DAs for the purposes of Paper II. For a full description of spectral classes of WDs and their meaning, see table 4.1[2] This explanation has shown to be able to explain the CMD bifurcation very well in works like that of Kilic et al. (2018, 2020) and Gentile Fusillo et al. (2019). Another recent discovery about the WDs is that their mass distribution is bimodal, with a main Gaussian centred on $\sim 0.6\ M_\odot$ and a secondary, smaller Gaussian around $\sim 0.8\ M_\odot$ (e.g., El-Badry et al. 2018; Kilic et al. 2018, 2020). This led to the expla-

[2]The 'D' in the spectral classifications stands for degenerate.

Table 4.1: Spectral classification of white dwarfs. The name of the spectral class and its definition.

Spectral class	Definition
DA	Hydrogen dominated spectrum
DB	Helium dominated spectrum
DC	Continuous spectrum, featureless
DO	He II and He I or H features
DZ	Metal lines dominate spectrum
DQ	Carbon lines dominate spectrum

nation **b**) that the second sequence could consist of heavier mass WDs, which have fainter and bluer cooling tracks. In single-star evolution, the more massive WDs would come from more massive progenitors, which then become WDs much on shorter timescales. For this reason, they would have colder kinematics due to the age-dispersion relation (Aumer et al., 2016). Mergers were suggested as a source of massive WDs but was ruled out by Kilic et al. (2020) who failed to discover significant massive WDs with hot kinematics. Instead El-Badry et al. (2018) shows that with the right choice of initial-final mass relation and continuous star formation, the second sequence can be populated by late-forming WDs. In summary, the second sequence can be explained as massive WDs formed recently. The two scenarios can be distinguished by their kinematics. The atmospheric composition should not have any bearing on the kinematics while, as explained above, the mass of WDs does. Therefore, we can investigate the kinematics of the two populations and try to provide insight into the cause of the CMD bifurcation.

4.3 Inferring f_v

As shown in Dehnen & Binney (1998), the mean motion $\langle \boldsymbol{v} \rangle$ and velocity dispersion $\boldsymbol{\sigma}$ can be determined for a sample of stars given a few caveats. The on-sky positions have to be uncorrelated with the velocities, which means that we see the same velocity distribution regardless of where on the sky we look. Consider the regions shown in Fig. 4.2. If there is a general mean motion for all parts of the sky, the line-of-sight motion of the red region will be given by the tangential motion of either pink or green regions in the direction of the red region, shown here using red arrows on the pink/green regions. Conversely, the tangential motion components of the red region that points to the left and right will give, approximately, the line-of-sight motion of the other two components, as indicated by the

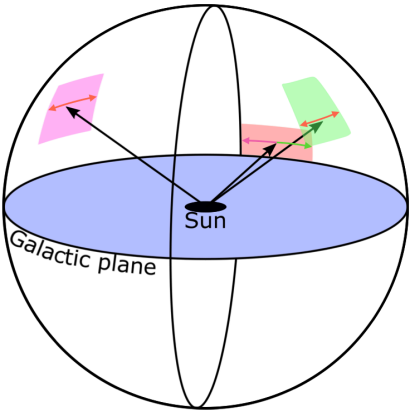

Figure 4.2: An illustration of positions on the celestial sphere from the point of view of a Solar system observer.

colouring of the arrows.

The same concept was used for the even more impressive feat of inferring the velocity distribution of Hipparcos stars in Dehnen (1998). We can write the probability distribution of tangential or transverse velocities in a given direction $\hat{\boldsymbol{r}}$ as $\rho(\boldsymbol{q}|\hat{\boldsymbol{r}})$ where $\boldsymbol{q}$ is the 2D vector of tangential velocities. To relate this distribution to the full velocity distribution we can write

$$\rho(\boldsymbol{q}|\hat{\boldsymbol{r}}) = \int \mathrm{d}v_r f(\boldsymbol{v}) = \int \mathrm{d}v_r f(\boldsymbol{p} + v_r\hat{\boldsymbol{r}}), \tag{4.1}$$

where $\boldsymbol{p}$ is the 3D projection of the tangential motion. The true distribution can of course not be determined precisely using transverse motion alone but it can be estimated with a log-likelihood maximization of some model of it. We do this numerically by defining the velocity distribution to be

$$f(\boldsymbol{v}) = e^{\phi(\boldsymbol{v})}, \tag{4.2}$$

where $\phi(\boldsymbol{v})$ is given on a 3D velocity grid with $L_U \times L_V \times L_W$ cells with widths $h_U \times h_V \times h_W$. The final expression for the function we seek to maximize, as a function of $\phi(\boldsymbol{v})$, is:

$$\tilde{\mathscr{L}}_\alpha(\boldsymbol{\phi}) = \overbrace{N^{-1}\sum_k \ln\left[\sum_{\boldsymbol{l}} e^{\phi_{\boldsymbol{l}}} K(k|\boldsymbol{l})\right]}^{\text{Sum of PDF}} - \underbrace{\sum_{\boldsymbol{l}} e^{\phi_{\boldsymbol{l}}}}_{\text{Normalizing term}} - \overbrace{\frac{1}{2}\alpha h_x h_y h_z \sum_{\boldsymbol{l}}\left(\sum_{\boldsymbol{n}} \phi_{\boldsymbol{n}} \Xi_{\boldsymbol{nl}}\right)^2}^{\text{penalizing term}}. \tag{4.3}$$

Here, N is the sample size, α is the smoothing parameter, $(\sum_{\boldsymbol{n}} \phi_{\boldsymbol{n}} \Xi_{\boldsymbol{nl}})$ is a numerical approximation for the second derivative of $\phi(\boldsymbol{v})$ for a given cell. This term, therefore, penalizes unsmooth solutions and is scaled by the smoothing parameter, α. For each star k, $K(k|\boldsymbol{l})$ is the length of the line $(\boldsymbol{p} + v_r \hat{\boldsymbol{r}})$ in velocity space through each cell, $\boldsymbol{l}$, formed by its tangential velocity and all possible radial velocities.

To determine α, we make use of a calibration sample of main sequence stars in the Solar neighbourhood that had measured radial velocities from *Gaia* DR2. We select some reasonable range of test values for α and run the maximization on this sample. Since we know the velocity distribution of this calibration sample, we can then choose the α that best reproduces it. Since the best choice of α depends on sample size, the calibration sample is picked so as to have about the same number of sources as the WD sample and uses an identical grid.

We chose a grid of $\boldsymbol{n} = [100, 100, 72]$ cells with velocity ranges:

$$\begin{aligned} U \in & [-150, 150] \text{ km s}^{-1} \\ V \in & [-150, 50] \text{ km s}^{-1} \\ W \in & [-80, 60] \text{ km s}^{-1}, \end{aligned}$$

which provides a resolution of about $\Delta v = [3, 2, 2]$ km s^{-1}. The algorithm is also set up to use a so-called multigrid approach, where the solution is first found on a coarser grid which is interpolated and used as an initial guess for the maximization on a finer grid. This refinement occurs $3 - 5$ times depending on the grid size.

We split the WD sample along the bifurcation in the colour-magnitude diagram (between 12th and 14th magnitude where it is strongest) as well as into three equally sized magnitude bins, which we simply call *A*, *B*, and *C* from brightest to faintest. The resulting velocity distributions in (U, V) are seen in Fig. 4.3. While the other velocity projections are also calculated (and shown in the paper) the (U, V) space shows the most structure. The overall shape can be quickly identified to match well with the known distribution of the main-sequence stars as seen in Fig. 3.2. The magnitude bins can be seen increasing in velocity dispersion as they go from *A* to *C*, reflecting the age-dispersion relation. As the dispersion becomes larger, *C* appears to have arch-like features as well, marked in the plot with red lines. The relative distributions on the third row have an unexpected result. We naturally would expect the more centrally fixated samples *A* and *B* to dominate close to the origin and *C* would dominate further out. This is mostly the case apart from a small region around $(U, V) \approx (7, -19)$ km s^{-1}. The region does not match conclusively with any known moving group and only Kushniruk et al.

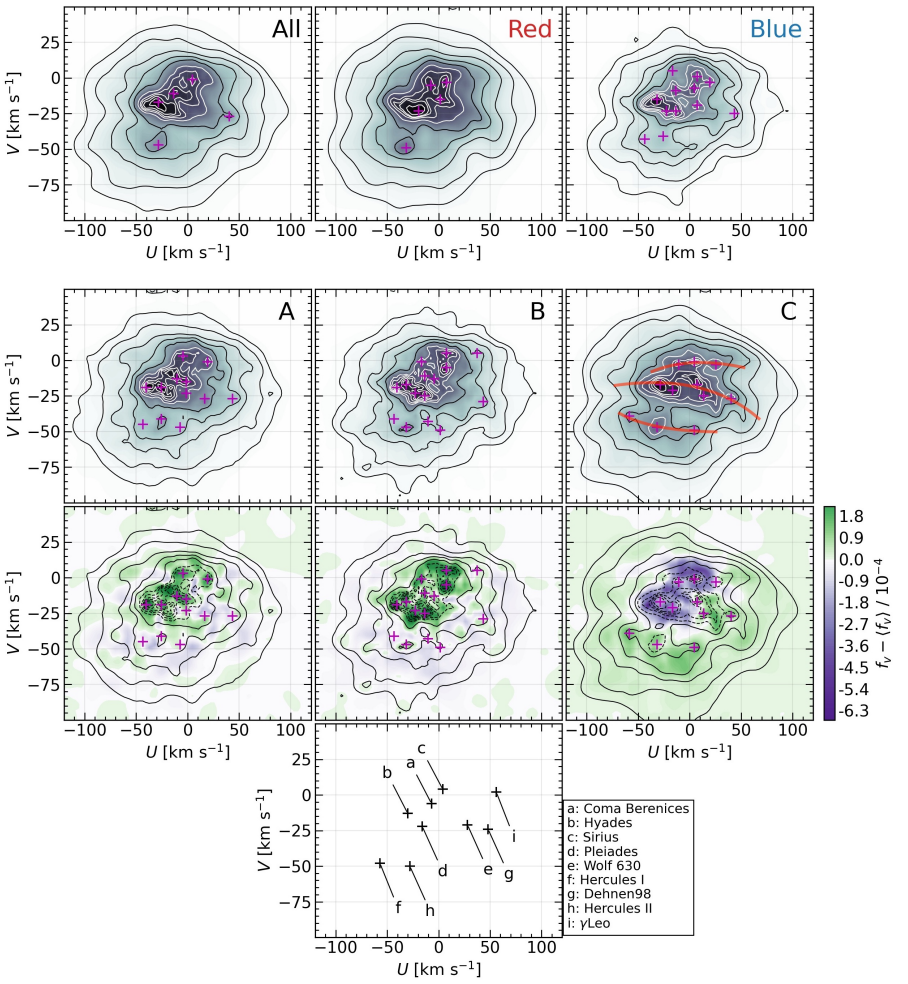

Figure 4.3: Velocity distributions of the WDs in the $U - V$ plane. Purple crosses show identified features. Shown also are the different sub-samples with the top row showing the different bifurcated sequences, the middle row shows the magnitude bins mentioned in section 4.3. The bottom row shows the distribution of the same magnitude bins subtracted by the mean of the three distributions, to highlight where each bin is strongest or weakest. At the bottom are shown the first nine groups identified in Antoja et al. (2012) for comparison.

(2017) provides a nearby link to *Coma Berenices* which has a suggested dynamical origin from a pericenter passing of the *Sagittarius* dwarf galaxy in Monari et al. (2018).

The regions on either side of the CMD bifurcation are seen in the top row and show similar dynamical features. However, the velocity dispersion of the red

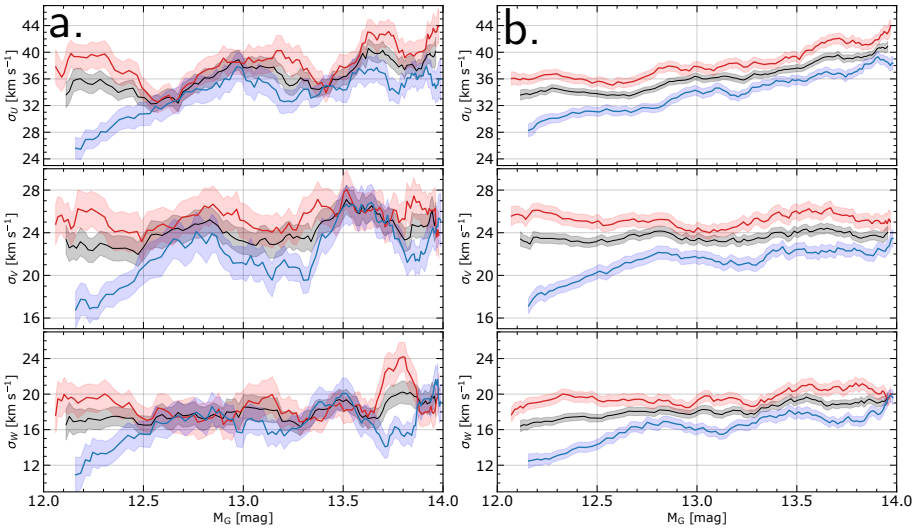

Figure 4.4: Moving velocity dispersion calculated in the three directions of U, V, and W, for the bifurcated sequences between 12th and 14th magnitude where they are visible. *a.* shows the moving dispersion for the red and blue sequences as well as the joint sample using WDs which are closer than 100 pc. The shaded regions show the 1σ uncertainty regions. *b.* same as the a. but for WDs up to 200 pc. Both plots show clearly a separation between the red and blue samples and when the 200 pc sample is used, they barely even overlap within 1σ.

sample is clearly larger than the blue. This hints at hotter kinematics and as such, we look to the dispersion of the samples rather than the full distribution for further analysis.

4.4 Two kinematic populations

We use the same method as in Dehnen & Binney (1998) to determine the velocity dispersion for a sample of stars. But we also employ a moving window across the CMD bifurcation to better compare the sequences as they cool. The velocity distributions shown in Fig. 4.3 were found for WDs within 500 pc, whereas here we use WDs limited to either 100 pc or 200 pc, the result of which can be seen in Fig. 4.4. Here it can be clearly seen for the 200 pc sample that the red sequence has a higher velocity dispersion across all magnitudes. For the 100 pc sample, this is also visible but less so. We can however show that the two samples are drawn

from the same underlying distribution. We determine the following Q-statistic for the two dispersion of the samples at various points:

$$Q = \frac{\sigma_{d_1} - \sigma_{d_2}}{\sqrt{\Delta\sigma_{d_1}^2 + \Delta\sigma_{d_2}^2}}, \tag{4.4}$$

where d_1 is the 100 pc sample and d_2 are stars between 100-200 pc. Both the red and blue Cumulative Distribution Functions (CDF) match well with a Gaussian distribution, and using a Kolmogorov-Smirnov test gives P-values between them and a true Gaussian which all lie above 0.8. Therefore, the difference between the two figures is consistent with simple statistical noise.

This shows that the two sequences between magnitudes 12 and 14 are *kinematically separate and distinct populations*. In regards to the discussion in section 4.2, this would agree neatly with the two sequences being comprised of WDs different masses where the heavier WDs are formed recently, giving them less time to be heated dynamically and thus forming the blue sample we have seen here. It cannot be ruled out the atmospheric composition is partly responsible for the bifurcation in the CMD but it cannot be the sole explanation. In our 100 pc samples, we cross-matched with the Montreal White Dwarf Database (Dufour et al., 2017) to find that 85% of the cross-matched red sample and 39% of the blue are DAs, so there are undoubtedly non-DAs in the second sequence. If they truly correspond to 60%, they still do not significantly alter the kinematics of the sample as a whole. It can be argued that the crystallization of massive WDs would provide massive WDs which are still visible in our range due to cooling delays (e.g., Tremblay et al. 2019; Bergeron et al. 2019; Bauer et al. 2020). If this were the case, these massive WDs would have been around for long enough to have significant dynamical heating. If this process is contaminating the sample, the fact that we still see the kinematic split is arguably even more significant.

Further insight into the CMD bifurcation of the WD sequence will likely require a combination of both spectroscopic and kinematic studies. Here, we have demonstrated the possibilities of working with only proper motions when analysing the vast Gaia datasets.

Chapter 5

Paper III

5.1 Introduction

Following on from the previous paper, we wished to apply our implemented MPLE to other interesting subsamples of the *Gaia* data. We were also able to make use of the improved Gaia DR3.

The study of kinematic space can be divided into the study of the Galactic disc and the stellar halo. This division guides our choice of samples and is understandable since the two regions are affected by different dynamical processes. The disc we have already described in section 4.1. The stellar halo, on the other hand, is where the evidence of past mergers between the Galaxy and its neighbours will be found (Helmi, 2020). These mergers can, for example, contribute to the velocity distribution and cause enhanced star formation (Ruiz-Lara et al., 2020). This is what inspires our chosen samples of data: the Solar neighbourhood disc sample and the local stellar halo.

Since our method requires only measured astrometry for the stars and not radial velocities, we can then utilise larger sets of data for these populations. Limiting the Solar neighbourhood to $\varpi > 5$ mas (or 200 pc) we can use as many as 1 171 846 stars, after having applied all of our quality cuts. This is comparable to current results using the Gaia RVS like Lucchini et al. (2022) which has 982 879 stars in the Solar neighbourhood. However, they do not apply any quality filters on photometry or astrometry, apart from a criteria of 20% parallax uncertainty ($\varpi/\sigma_\varpi > 5$). We restrict our results to only 10% uncertainty and if we were to use 20%, we would have 3 592 434 sources before applying our quality filters, which highlights the benefits of our method.

For the stellar halo, a recent similar sample is Dodd et al. (2022) which limits their halo to 2.5 kpc with <20% relative parallax uncertainty as well as imposing a velocity cut whereby the motions of the star with respect to the Local Standard of Rest (LSR) must be greater than 210 km/s. Since the circular speed at the position of the sun is ∼233 km s^{-1} (McMillan, 2017), this cut removes the vast majority of the disc stars. Our cuts on distance and velocity are slightly more generous with a distance limit of 3 kpc and velocity limit of at least 200 km s^{-1}, albeit on transverse velocity rather than full space velocity. Their sample contains 72 274 stars, whereas ours contains 456 273.

We use these two samples to estimate their velocity distributions. For the Solar neighbourhood, this is done in the same manner as for the WDs in the previous paper. The stellar halo distribution is inferred in spherical coordinates rather than Cartesian since it is more spherically symmetric around the Galaxy. We also divide the stellar halo into *in situ* and *accreted* components (e.g., Naidu et al. 2020). The velocity distributions are studied closely to determine if known structure is detected and what new structure we are able to identify. Some novel structures do appear in our analysis, specifically in the accreted halo where we find two new features that we call *MMH-1* and *MMH-2*.

5.2 Gaia's view of the local Galaxy

There has been plenty of work done to try and characterise the velocity substructure that exists in the disc and stellar halo. We briefly discussed the Solar neighbourhood in chapter 4 and showed several moving groups from Antoja et al. (2012) in Fig. 4.3. Above Lucchini et al. (2022) was mentioned which is one of the more recent works that investigates the disc structure. The current picture of the local disc velocity distribution is one with multiple arch-like structures, of which many fractured individual substructures can be identified (see e.g., Table 1 from Lucchini et al. 2022).

For the stellar halo, things look slightly different. This is currently a very active field, but some smaller discoveries were made already 20 years ago using Hipparcos to identify the Helmi streams (Helmi et al., 1999). It is, perhaps, not surprising that *Gaia* has had a significant impact on this field as well. When DR2 was released, an important finding for the stellar halo came soon thereafter. By selecting stars with $v_{\mathrm{T}} > 200$ km s^{-1} Gaia Collaboration et al. (2018b) showed that in the CMD appears two separate main sequences, a finding that we recreate and show in Fig. 5.1. Rather than a main sequence with binaries adding a brighter,

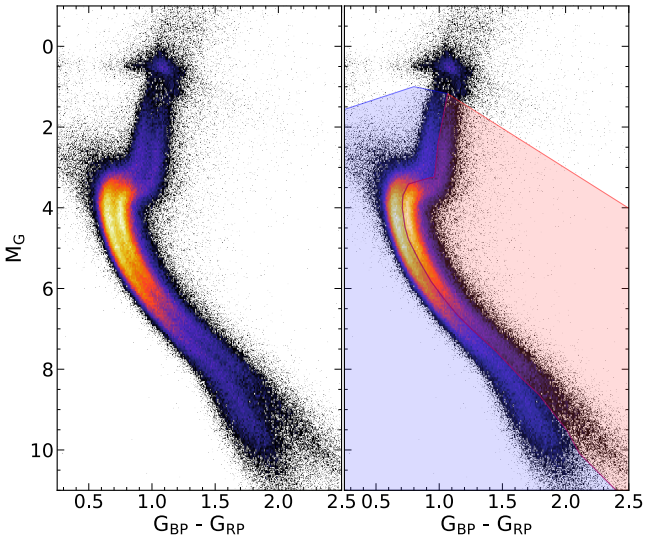

Figure 5.1: Colour-magnitude diagram of our filtered halo sample. The colour shows the number density. The right panel shows selected regions for the left and right sequences overlaid with shaded areas.

redder sequence the new sequence appears on the left, consistent with isochrones of a lower metallicity. Based on its kinematics, chemistry, and age the left sequence was found to be connected to an accretion event from a single object (Belokurov et al., 2018; Helmi et al., 2018) which is called *Gaia-Sausage-Enceladus* or *GSE*. This led to a successful hunt for other accreted populations in the stellar halo which matched very well to the notion of a Galaxy formed through hierarchical growth, suggested by the ΛCDM model mentioned in Section 1.1.3. At the time of writing, some of the larger discovered structures include *Sequoia* (Myeong et al., 2019), *Antaeus* (Oria et al., 2022), *Thamnos* 1 and 2 (Koppelman et al., 2019), and *Typhon* (Tenachi et al., 2022), to name a few. We show the expected positions of these features as well as some smaller ones in Fig. 5.2. This puts into perspective how structured the Galactic stellar halo has been revealed to be with the use of *Gaia* data.

Since we have access to the most expansive catalogue of sources from *Gaia*, we aim to expand the view of substructure in the local parts of the Galaxy's disc and stellar halo.

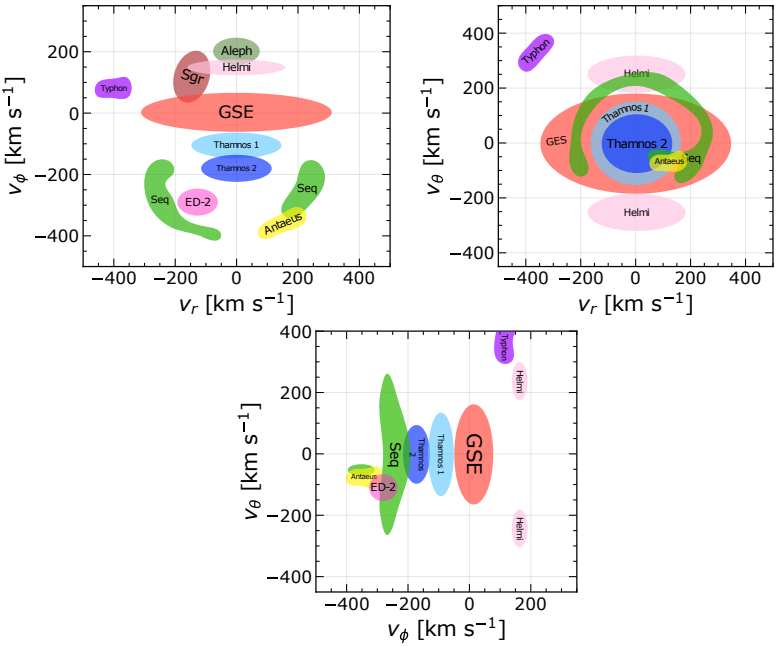

Figure 5.2: Estimated typical positions of known velocity structures in the stellar halo. Figures show the velocity spaces of (v_r, v_ϕ) (top left), (v_r, v_θ) (top right), and (v_ϕ, v_θ) (bottom). Here v_r points outwards from the Galactic centre, v_ϕ increases in the direction of Galactic rotation, and v_θ increases from south to north Galactic poles.

5.3 Structures: The old and the new

When we investigated the velocity distribution of the Solar neighbourhood we found that the distribution is heavily dominated by the typical major moving groups: *Sirius*, *Coma Berencies*, *Hyades*, *Pleiades*, and *Hercules*. The distributions also contains weaker traces of *Dehnen98* and *Wolf630*. A curious feature that stood out is a strong overdensity near *Pleiades*, close to $(U, V) = (-10, -15)$ km s^{-1} which is not found in literature. This may be a new moving group that we can discern due to our 1 km s^{-1} resolution. However, since the distribution is so heavily dominated by the major features, a better way of unravelling the low-level structure that these representations of the velocity distribution may have missed is to renormalize the plots. This implies that rather than showing the full 2D probability density of U and V, we show the *conditional* probabilities of V or U

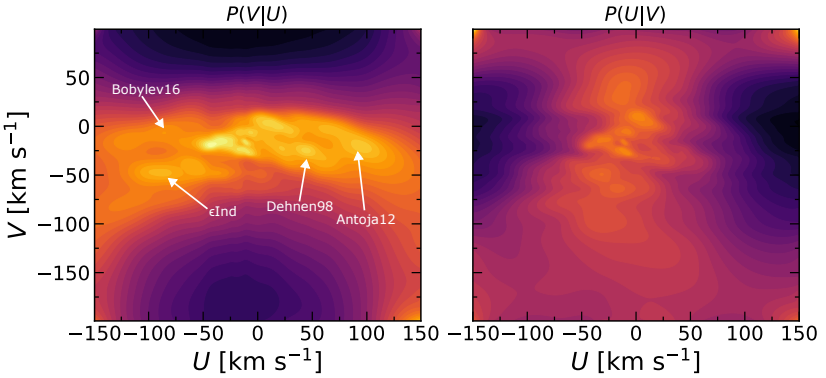

Figure 5.3: The conditional probability of one velocity component in (U, V) against the other. Left shows $P(V|U)$ and right shows $P(U|V)$ which reveals rich substructure beyond the central dominating groups. The color shows the density scaled as $P(v)^{0.25}$.

for each U or V, respectively. That is, the colour represents the probability of the star having a specific V given that it has a certain U velocity (or vice versa). The result is probability maps that can reveal structure that is otherwise blotted out by the major groups and we show this in Fig. 5.3. Here can be seen much richer structure like *ϵInd* (e.g., Antoja et al. 2012; Kushniruk et al. 2017; Bobylev & Bajkova 2016) at $(U, V) = (-100, -50)$ km s^{-1}, *Dehnen98* (Antoja et al., 2012) at $(U, V) = (50, -30)$ km s^{-1}, a group from Bobylev & Bajkova (2016) at $(U, V) = (-100, -10)$ km s^{-1}, and likely *Antoja12* from e.g. Kushniruk et al. (2017) at $(U, V) = (100, -30)$ km s^{-1}. The conditional probability maps are clearly a useful tool for the outer regions.

The velocity distributions of the two halo samples were determined and as expected, the right sequence shows very little accreted structure and as such we only focus on the left sequence. The velocity distributions are shown in Fig. 5.4 and are overlaid with the expected positions of stellar halo substructure from Fig. 5.2. These distributions show clearly a lot of the known velocity substructures such as *GSE*, *Sequoia*, and the *Helmi* streams. Particularly the *GSE* in (v_r, v_ϕ) shows a lot of structure with significant peaks marked as G1-G5. The groups at largest v_r, 1 and 5, are placed where the *GSE* is typically associated (e.g., Feuillet et al. 2021). G2 and G4 lie near the region which is removed by our cut of $v_\mathrm{T} < 200$ km s^{-1} and are therefore probably contaminants from the disc population. Finally G3 matches with Cluster 3 of Lövdal et al. (2022) which is also called *L-RL3* in Dodd

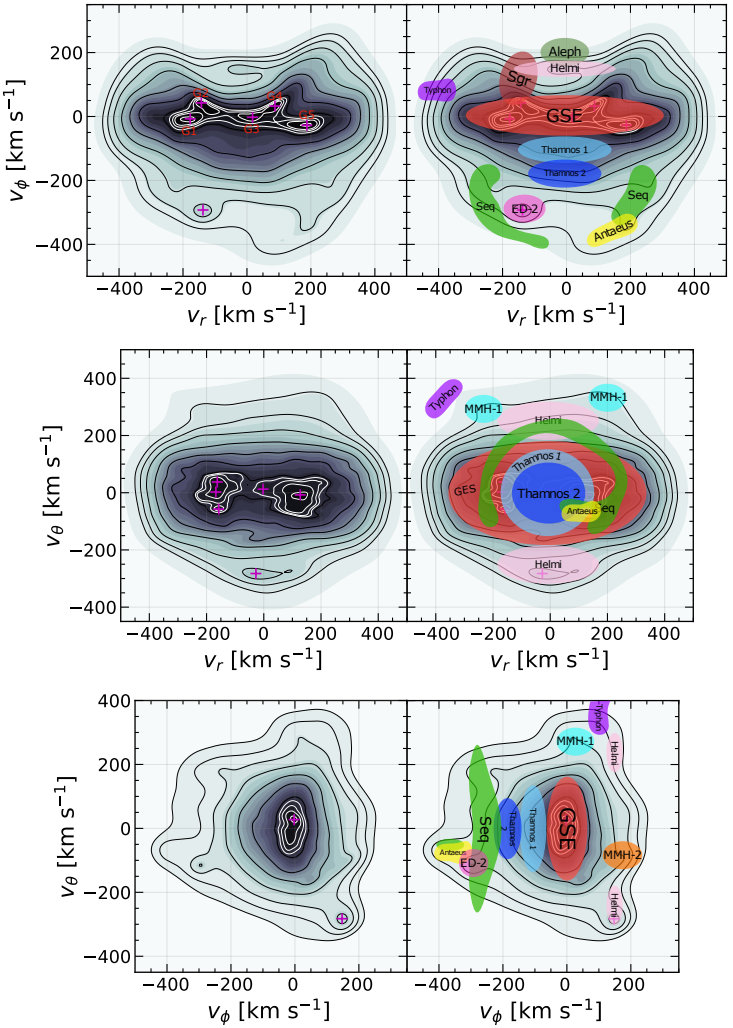

Figure 5.4: Velocity distributions of our left halo sample in (v_r, v_ϕ) (top row), (v_r, v_θ) (middle row), and $(v_\phi, v_\theta$ (bottom row). The right column shows the same distributions overlaid with the positions of expected substructures from literature, in a similar style to what is done in Naidu et al. (2020) and Mardini et al. (2022). Significant peaks are marked with purple crosses and in the top left figure five significant groups belonging to the *GSE* are marked as G1-G5.

et al. (2022). The distributions do show some of the smaller features as well and particularly the low v_θ-component of the *Helmi* stream is very pronounced here.

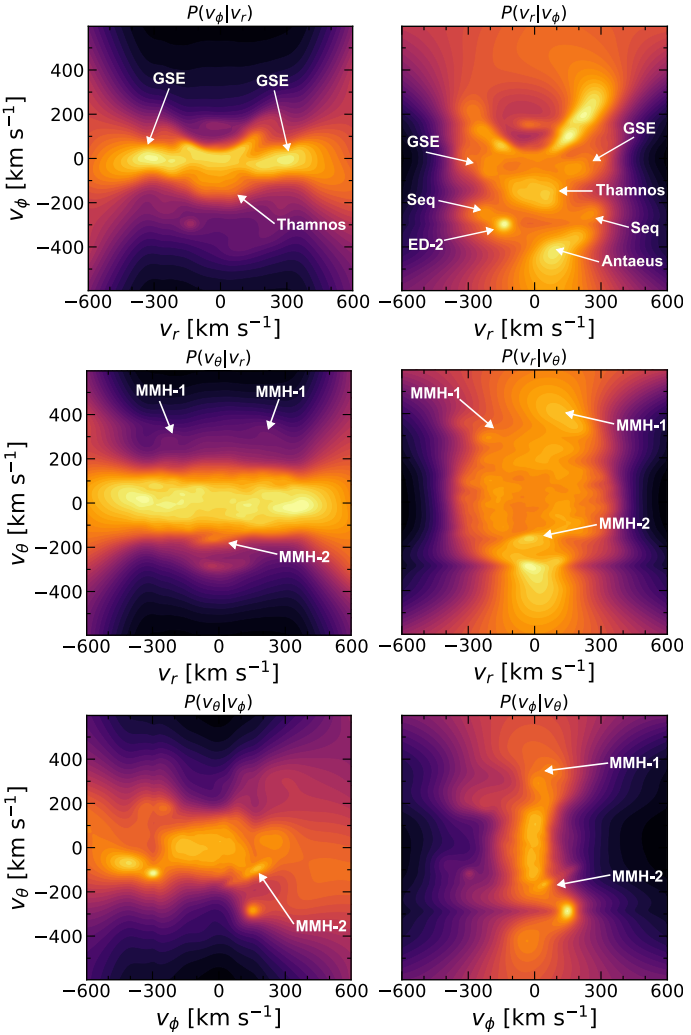

Figure 5.5: Conditional probability distributions of the velocities from Fig. 5.4 with the left column showing the conditional probability distribution of the y-axis velocity on the x-axis velocity. The right column shows the inverted conditional probabilities. Density is scaled as $P(v)^{0.25}$. The arrows show features discussed in Section 5.3. This map is used to unveil further information in the phase-space structure and as such the other features of Fig. 5.4 are not labelled here.

These figures give a good impression of what the accreted stellar halo looks like at

'face value'.

Beyond these larger structures, there are three additional ones that we are able to identify. The first is *ED-2* from Dodd et al. (2022) at roughly $(v_r, v_\phi, v_\theta) = (-150, -300, -100)$ km s^{-1}. In Dodd et al. (2022) they note that it occupies about 0.05% of their sample with 33 proposed members. This region of velocity space makes up around 0.075% in our sample, suggesting that the group is slightly larger than previously believed. We are also able to make out two new velocity features which we call *MMH-1* and *MMH-2* which have no prior associations in literature. The first, *MMH-1*, lies at about $(v_r, v_\phi, v_\theta) = (\pm 225, 25, 325)$ km s^{-1} and is visible in the spaces of (v_r, v_θ) and (v_ϕ, v_θ). It is placed in the dense regions in (v_r, v_ϕ) and is therefore difficult to spot there. The second is *MMH-2* which is around $(v_\phi, v_\theta) \approx (150, -100)$ km s^{-1} and is a challenge to trace into v_r. However, its v_r component became clear when we again looked to the conditional probability of the velocities, seen in Fig. 5.5. Here, the sloped feature centred around $(v_r, v_\theta) = (0, -150)$ km s^{-1} stands out in both $P(v_r|v_\theta)$ and $P(v_\theta|v_r)$, and is the representation of *MMH-2* in this space. This shows also that the full extent of *MMH-2* is obscured in Fig. 5.4 and that its actual velocities are instead centred on $(v_r, v_\phi, v_\theta) = (0, 150, -125)$ km s^{-1}. These maps also reveal some parts of *Thamnos* up to $(v_r, v_\phi) = (0, -200)$ km s^{-1} which could previously not be seen. The extended nature of *MMH-1* at $v_\theta = 300$ km s^{-1} is uncovered as well, stretching to even larger values of v_θ in both $P(v_r|v_\theta)$ and $P(v_\phi|v_\theta)$ and has what appears to be a symmetrical component at large negative v_θ, which if real would likely imply that this feature has considerable vertical action. This view also shows the strength of *MMH-1* as it appears in both $P(v_\theta|v_\phi)$ and $P(v_\phi|v_\theta)$.

The distributions and the insight into the Galaxy that we gain from them clearly advocate for the benefits of working with pure proper-motion limited catalogues. Until such a time that comparable 6D catalogues are available, these types of methods provide the largest possible data sets for kinematic studies.

References

Andersson E. P., Agertz O., Renaud F., 2020, MNRAS, 494, 3328

Anguiano B., Rebassa-Mansergas A., García-Berro E., Torres S., Freeman K. C., Zwitter T., 2017, MNRAS, 469, 2102

Antoja T., Figueras F., Torra J., Valenzuela O., Pichardo B., 2010, in , Vol. 4, Lecture Notes and Essays in Astrophysics. pp 13–31

Antoja T., et al., 2012, MNRAS, 426, L1

Antoja T., de Bruijne J., Figueras F., Mor R., Prusti T., Roca-Fàbrega S., 2017, A&A, 602, L13

Aumer M., Binney J., Schönrich R., 2016, MNRAS, 462, 1697

Bauer E. B., Schwab J., Bildsten L., Cheng S., 2020, ApJ, 902, 93

Belokurov V., Erkal D., Evans N. W., Koposov S. E., Deason A. J., 2018, MNRAS, 478, 611

Bensby T., Feltzing S., Oey M. S., 2014, A&A, 562, A71

Bergeron P., Dufour P., Fontaine G., Coutu S., Blouin S., Genest-Beaulieu C., Bédard A., Rolland B., 2019, ApJ, 876, 67

Binney J., 2007, in DE JONG R. S., ed., ISLAND UNIVERSES. Springer Netherlands, Dordrecht, pp 67–76

Binney J., Tremaine S., 2008, Galactic Dynamics: Second Edition

Bland-Hawthorn J., Gerhard O., 2016, ARA&A, 54, 529

Bobylev V. V., Bajkova A. T., 2016, Astronomy Letters, 42, 90

Bovy J., Leung H. W., Hunt J. A. S., Mackereth J. T., García-Hernández D. A., Roman-Lopes A., 2019, MNRAS, 490, 4740

Burbidge E. M., Burbidge G. R., Fowler W. A., Hoyle F., 1957, Reviews of Modern Physics, 29, 547

Clarke J. P., Gerhard O., 2022, MNRAS, 512, 2171

Clarkson W., et al., 2008, ApJ, 684, 1110

D'Onghia E., 2015, ApJL, 808, L8

Da Costa G. S., et al., 2019, MNRAS, 489, 5900

Daniel K. J., Wyse R. F. G., 2018, MNRAS, 476, 1561

Dehnen W., 1998, AJ, 115, 2384

Dehnen W., Binney J. J., 1998, MNRAS, 298, 387

Dehnen W., McLaughlin D. E., 2005, MNRAS, 363, 1057

Dodd E., Callingham T. M., Helmi A., Matsuno T., Ruiz-Lara T., Balbinot E., Lovdal S., 2022, arXiv e-prints, p. arXiv:2206.11248

Dufour P., Blouin S., Coutu S., Fortin-Archambault M., Thibeault C., Bergeron P., Fontaine G., 2017, in Tremblay P. E., Gaensicke B., Marsh T., eds, Astronomical Society of the Pacific Conference Series Vol. 509, 20th European White Dwarf Workshop. p. 3 (arXiv:1610.00986)

Edvardsson B., Andersen J., Gustafsson B., Lambert D. L., Nissen P. E., Tomkin J., 1993, A&A, 275, 101

Eisenhauer F., et al., 2011, The Messenger, 143, 16

El-Badry K., Rix H.-W., Weisz D. R., 2018, ApJL, 860, L17

Fall S. M., Efstathiou G., 1980, MNRAS, 193, 189

Feuillet D. K., Sahlholdt C. L., Feltzing S., Casagrande L., 2021, MNRAS, 508, 1489

Flamsteed J., 1725, Historia Coelestis Britannicae

Fontaine G., Brassard P., Bergeron P., 2001, PASP, 113, 409

Frankel N., Rix H.-W., Ting Y.-S., Ness M., Hogg D. W., 2018, ApJ, 865, 96

Gaia Collaboration et al., 2016a, A&A, 595, A1

Gaia Collaboration et al., 2016b, A&A, 595, A2

Gaia Collaboration et al., 2018a, A&A, 616, A1

Gaia Collaboration et al., 2018b, A&A, 616, A10

Gaia Collaboration et al., 2018c, A&A, 616, A11

Gaia Collaboration et al., 2021, A&A, 649, A1

Gaia Collaboration et al., 2022a, A&A accepted, arXiv:2206.06207

Gaia Collaboration et al., 2022b, A&A accepted, arXiv:2208.00211

Gentile Fusillo N. P., et al., 2019, MNRAS, 482, 4570

Halle A., Di Matteo P., Haywood M., Combes F., 2015, A&A, 578, A58

Hayden M. R., et al., 2015, ApJ, 808, 132

Helmi A., 2020, ARA&A, 58, 205

Helmi A., White S. D. M., de Zeeuw P. T., Zhao H., 1999, Nature, 402, 53

Helmi A., Babusiaux C., Koppelman H. H., Massari D., Veljanoski J., Brown A. G. A., 2018, Nature, 563, 85

Hernquist L., 1990, ApJ, 356, 359

Hobbs D., et al., 2021, Experimental Astronomy, 51, 783

Høg E., et al., 2000, A&A, 355, L27

Horta D., et al., 2022, arXiv e-prints, p. arXiv:2204.04233

Katz D., Gómez A., Haywood M., Snaith O., Di Matteo P., 2021, A&A, 655, A111

Kilic M., Hambly N. C., Bergeron P., Genest-Beaulieu C., Rowell N., 2018, MNRAS, 479, L113

Kilic M., Bergeron P., Kosakowski A., Brown W. R., Agüeros M. A., Blouin S., 2020, ApJ, 898, 84

Kippenhahn R., Weigert A., Weiss A., 2012, Stellar Structure and Evolution. Springer Science & Business Media

Kipper R., Tenjes P., Tuvikene T., Ganeshaiah Veena P., Tempel E., 2020, MNRAS, 494, 3358

Koppelman H. H., Helmi A., 2021, A&A, 649, A136

Koppelman H. H., Helmi A., Massari D., Price-Whelan A. M., Starkenburg T. K., 2019, A&A, 631, L9

Kormendy J., 2013, in Falcón-Barroso J., Knapen J. H., eds, , Secular Evolution of Galaxies. p. 1

Kushniruk I., Schirmer T., Bensby T., 2017, A&A, 608, A73

Leeming D. A., 1998, Mythology: The Voyage of the Hero. Oxford University Press

Lövdal S., Ruiz-Lara T., Koppelman H. H., Matsuno T., Dodd E., Helmi A., 2022, arXiv e-prints, p. arXiv:2201.02404

Lucchini S., Pellett E., D'Onghia E., Aguerri J. A. L., 2022, arXiv e-prints, p. arXiv:2206.10633

Mackereth J. T., Bovy J., 2020, MNRAS, 492, 3631

Magli G., 2020, Archaeoastronomy: introduction to the science of stars and stones. Springer Nature

Mardini M. K., Frebel A., Chiti A., Meiron Y., Brauer K. V., Ou X., 2022, ApJ, 936, 78

Martig M., Minchev I., Flynn C., 2014, MNRAS, 443, 2452

Martig M., Minchev I., Ness M., Fouesneau M., Rix H.-W., 2016, ApJ, 831, 139

McMillan P. J., 2017, MNRAS, 465, 76

McMillan P. J., Dehnen W., 2007, MNRAS, 378, 541

McMillan P. J., et al., 2022, MNRAS,

Michalik D., Lindegren L., Hobbs D., 2015, A&A, 574, A115

Minchev I., Famaey B., Quillen A. C., Di Matteo P., Combes F., Vlajić M., Erwin P., Bland-Hawthorn J., 2012, A&A, 548, A126

Monari G., et al., 2018, Research Notes of the American Astronomical Society, 2, 32

Myeong G. C., Vasiliev E., Iorio G., Evans N. W., Belokurov V., 2019, MNRAS, 488, 1235

Naidu R. P., Conroy C., Bonaca A., Johnson B. D., Ting Y.-S., Caldwell N., Zaritsky D., Cargile P. A., 2020, ApJ, 901, 48

Ness M., et al., 2013a, MNRAS, 430, 836

Ness M., et al., 2013b, MNRAS, 432, 2092

Ness M., Debattista V. P., Bensby T., Feltzing S., Roškar R., Cole D. R., Johnson J. A., Freeman K., 2014, ApJL, 787, L19

Oria P.-A., Tenachi W., Ibata R., Famaey B., Yuan Z., Arentsen A., Martin N., Viswanathan A., 2022, ApJL, 936, L3

Perryman M., 2009, Astronomical Applications of Astrometry: Ten Years of Exploitation of the Hipparcos Satellite Data. Cambridge University Press

Perryman M., 2012, European Physical Journal H, 37, 745

Perryman M. A. C., et al., 1997, A&A, 323, L49

Planck Collaboration et al., 2020, A&A, 641, A6

Posti L., Helmi A., 2019, A&A, 621, A56

Raddi R., et al., 2022, A&A, 658, A22

Reid M. J., et al., 2019, ApJ, 885, 131

Roškar R., Debattista V. P., Quinn T. R., Wadsley J., 2012, MNRAS, 426, 2089

Rowell N., Hambly N. C., 2011, MNRAS, 417, 93

Ruiz-Lara T., Gallart C., Bernard E. J., Cassisi S., 2020, Nature Astronomy, 4, 965

Sanders J. L., Smith L., Evans N. W., 2019, MNRAS, 488, 4552

Schönrich R., Binney J., 2009, MNRAS, 396, 203

Schönrich R., McMillan P. J., 2017, MNRAS, 467, 1154

Sellwood J. A., Binney J. J., 2002, MNRAS, 336, 785

Shen J., Rich R. M., Kormendy J., Howard C. D., De Propris R., Kunder A., 2010, ApJL, 720, L72

Sion E. M., Liebert J., 1977, ApJ, 213, 468

Sion E. M., Fritz M. L., McMullin J. P., Lallo M. D., 1988, AJ, 96, 251

Solway M., Sellwood J. A., Schönrich R., 2012, MNRAS, 422, 1363

Springel V., et al., 2005, Nature, 435, 629

Tenachi W., Oria P.-A., Ibata R., Famaey B., Yuan Z., Arentsen A., Martin N., Viswanathan A., 2022, ApJL, 935, L22

Teuben P., 1995, in Shaw R. A., Payne H. E., Hayes J. J. E., eds, Astronomical Society of the Pacific Conference Series Vol. 77, Astronomical Data Analysis Software and Systems IV. p. 398

Torres S., Cantero C., Camisassa M. E., Antoja T., Rebassa-Mansergas A., Althaus L. G., Thelemaque T., Cánovas H., 2019, A&A, 629, L6

Toyouchi D., Chiba M., 2016, ApJ, 833, 239

Tremblay P.-E., et al., 2019, Nature, 565, 202

Trick W. H., 2022, MNRAS, 509, 844

Trick W. H., Coronado J., Rix H.-W., 2019, MNRAS, 484, 3291

Trick W. H., Fragkoudi F., Hunt J. A. S., Mackereth J. T., White S. D. M., 2021, MNRAS, 500, 2645

Vera-Ciro C., D'Onghia E., Navarro J., Abadi M., 2014, ApJ, 794, 173

Vera-Ciro C., D'Onghia E., Navarro J. F., 2016, ApJ, 833, 42

Wegg C., Gerhard O., 2013, MNRAS, 435, 1874

Wegg C., Gerhard O., Portail M., 2015, MNRAS, 450, 4050

White S. D. M., Rees M. J., 1978, MNRAS, 183, 341

Wright T., 1750, An original theory or new hypothesis of the universe: founded upon the laws of nature, and solving by mathematical principles the general phnomena of the visible creation; and particularly the via lactea

Xu Y., et al., 2013, ApJ, 769, 15

Zari E., Frankel N., Rix H. W., 2022, arXiv e-prints, p. arXiv:2206.02616

de Jong T., 2007, Wiener Zeitschrift für die Kunde des Morgenlandes, 97, 107

de Lalande J. J. L. F., 1801, Histoire céleste française. Vol. 1

van Altena W. F., Lee J. T., Hoffleit E. D., 1995, The general catalogue of trigonometric [stellar] parallaxes

Scientific publications

Printed by Media-Tryck, Lund 2022 NORDIC SWAN ECOLABEL 3041 0903

Faculty of Science
Department of Astronomy
and Theoretical Physics

ISBN 978-91-8039-411-6